Paleoceanography and Paleoclimatology

RESEARCH ARTICLE
10.1029/2023PA004671

Key Points:

- We present new high resolution (3,000-year) leaf wax δ^2H data from central Kenya spanning 3.3–2.6 million years before present (Ma)
- Pronounced 41,000-year variability throughout is potentially attributable to the cross-equatorial insolation gradient
- Long-term (>200,000-year) variability in eastern African hydroclimate tracks the zonal Indian Ocean surface temperature gradient

Supporting Information:

Supporting Information may be found in the online version of this article.

Correspondence to:

B. A. Mitsunaga,
bryce_mitsunaga@brown.edu

Citation:

Mitsunaga, B. A., Lupien, R. L., Ouertani, S., Stubbs, B., Deino, A. L., Kingston, J. D., et al. (2023). High-latitude, Indian Ocean, and orbital influences on eastern African hydroclimate across the Plio-Pleistocene boundary. *Paleoceanography and Paleoclimatology*, *38*, e2023PA004671. https://doi.org/10.1029/2023PA004671

Received 2 MAY 2023
Accepted 3 NOV 2023

High-Latitude, Indian Ocean, and Orbital Influences on Eastern African Hydroclimate Across the Plio-Pleistocene Boundary

Bryce A. Mitsunaga[1], Rachel L. Lupien[2], Samantha Ouertani[1], Brandon Stubbs[1], Alan L. Deino[3], John D. Kingston[4], Mona Stockhecke[5], Erik T. Brown[5], and James M. Russell[1]

[1]Department of Earth, Environmental, and Planetary Sciences, Brown University, Providence, RI, USA, [2]Department of Geoscience, Aarhus University, Aarhus, Denmark, [3]Berkeley Geochronology Center, Berkeley, CA, USA, [4]Department of Anthropology, University of Michigan, Ann Arbor, MI, USA, [5]Large Lakes Observatory, University of Minnesota Duluth, Duluth, MN, USA

Abstract Terrestrial-marine dust fluxes, pedogenic carbonate $\delta^{13}C$ values, and various paleovegetation proxies suggest that Africa experienced gradual cooling and drying across the Pliocene-Pleistocene (Plio-Pleistocene) boundary (2.58 million years ago [Ma]). However, the timing, magnitude, resolution, and relative influences of orbitally-driven changes in high latitude glaciations and low latitude insolation differ by region and proxy. To disentangle these forcings and investigate equatorial eastern African climate across the Plio-Pleistocene boundary, we generated a high-resolution (~3,000-year) data set of compound-specific *n*-alkane leaf wax δ^2H values—a robust proxy for atmospheric circulation and precipitation amount—from the HSPDP-BTB13-1A core, which spans a ~3.3–2.6 Ma sequence in the Baringo-Tugen Hills-Barsemoi Basin of central Kenya. In combination with the physical sedimentology, our data indicate that precipitation varied strongly with orbital obliquity, not precession, during the late Pliocene, perhaps imparted by variations in the cross-equatorial insolation gradient. We also observe a marked shift toward wetter conditions beginning ~3 Ma that corresponds with global cooling, drying in western Australia, and a steepening of the west-east zonal Indian Ocean (IO) sea surface temperature (SST) gradient. We propose that northward migration of the Subtropical Front reduced Agulhas current leakage, warming the western IO and causing changes in the IO zonal SST gradient at 3 Ma, a process that has been observed in the latest Pleistocene-Holocene but not over longer timescales. Thus, the late Cenozoic moisture history of eastern Africa is driven by a complex mixture of low-latitude insolation, the IO SST gradient, and teleconnections to distal high-latitude cooling.

1. Introduction

The Pliocene and Pleistocene epochs (Plio-Pleistocene; 5.3–0 million years before present [Ma]) encompass several major climate state changes as well as transitions in the frequency and amplitude of climate cycles, including gradual high-latitude cooling, intensification of Northern Hemisphere glaciation (iNHG) (~2.75 Ma), and a progression from strongly 21,000-year (21-kyr) to 41- to 100-kyr periodicity in marine temperatures and ice volume (Herbert et al., 2010; Lisiecki & Raymo, 2005, 2007). Oceanic trends during the Plio-Pleistocene are well characterized, but until relatively recently, the dearth of long terrestrial records has limited our understanding of the evolution of continental climate (Table 1). Shifts in the secular trend and periodicity of eastern African hydroclimate across the Plio-Pleistocene are particularly important given their relationship to human evolution, and yet existing records are often conflicting, short, low-resolution, and/or concentrated in certain areas.

Offshore records of North African dust provided the first long, high-resolution records sensitive to terrestrial conditions. Dust concentrations were initially believed to increase around the Plio-Pleistocene boundary (deMenocal, 1995), suggesting that global cooling and ice volume growth caused African drying (although statistical reanalysis of dust records suggests no significant flux increases until ~2–1.5 Ma (Trauth et al., 2009)), in conjunction with northeastern African Miocene-Pliocene forests yielding to scrub- and grasslands around 2.5 Ma (Bonnefille, 1983; Cerling, 1992; Griffin, 1999; WoldeGabriel et al., 2001; Yemane et al., 1985). However, it has become increasingly apparent that African rainfall and vegetation may have different controls (Crocker et al., 2022; O'Mara et al., 2022; Polissar et al., 2019; Windler et al., 2023), such that paleo-vegetation and -hydroclimate proxies cannot be assumed to be linked in simple ways.

Paleoceanography and Paleoclimatology

10.1029/2023PA004671

Table 1
Locations, Sources, and Ages of Hydroclimate and SST Proxies

	Core	Location	Reference	Age (Ma)	Hydroclimate proxy	$\Delta SST_{W\text{-}E}$	SST proxy	Reference	$\Delta SST_{W\text{-}E}$ r	p	SST r	p
Pleistocene-Holocene	CD154-10-06P	Mozambique Channel	Simon et al. (2015)	0.269–0.002	XRF (Fe/K)	ODP 722-IODP U1461	$U^{k'}_{37}$	He et al. (2021) and Herbert et al. (2015)	**0.70**	**<0.005**		
	HSPDP-CHB14-2	Chew Bahir Basin	Foerster et al. (2022)	0.616–0.002	*XRF (K/Zr)*				**0.47**	**<0.05**		
	HSPDP-CHB14-2	Chew Bahir Basin	Lupien et al. (2022)	0.282–0.001	*δ^2H_{precip} (‰ VSMOW)*				**0.49**	**<0.05**		
	HSPDP-MAG14-2A	Lake Magadi	Owen et al. (2018)	1.041–0.002	*XRF (Na/Ca)*				**0.84**	**<0.001**		
	HSPDP-WTK13-1A	Turkana Basin	Lupien et al. (2018)	1.867–1.388	*δ^2H_{precip} (‰ VSMOW)*				−0.26	<0.5		
	MAL05-1	Lake Malawi	Johnson et al. (2016)	1.279–0.011	*XRF (Ca)*				**−0.75**	**<0.001**		
	MD96-2048	Limpopo River catchment	Caley et al. (2018)	2.141–0.001	XRF (Fe/Ca)				**0.52**	**<0.05**	−0.07	<0.5
	ODP-OLO12-1A	Olorgesailie/Koora Basin	Potts et al. (2020)	1.007–0.088	XRF (Si/K)				0.09	<1		
	Pretoria Saltpan	Pretoria Saltpan	Partridge et al. (1997)	0.197–0.000	Precipitation (mm/yr)				**0.51**	**<0.05**		
	RC09-166	Gulf of Aden	Tierney et al. (2017)	0.212–0.002	*δ^2H_{C30} (‰ VSMOW)*				**0.73**	**<0.001**	**0.52**	**<0.001**
	VM19-193	Western Indian Ocean	Windler et al. (2023)	0.247–0.008	*δ^2H_{C30} (‰ VSMOW)*				**0.56**	**<0.05**	**0.35**	**<0.001**
Plio-Pleistocene	DSDP Site 231	Gulf of Aden	Liddy et al. (2016)	5.239–2.159	*δ^2H_{C28} (‰ VSMOW)*	DSDP 231-IODP U1463	TEX_{86}	Liddy et al. (2016) and Smith and Castañeda (2020)	0.01	<1	**0.55**	**<0.001**
	IODP Site U1478	Limpopo River catchment	Taylor et al. (2021)	4.052–1.809	*δ^2H_{C28} (‰ VSMOW)*	IODP U1478-IODP U1463	TEX_{86}	Smith and Castañeda (2020) and Taylor et al. (2021)	**0.46**	**<0.05**	**0.49**	**<0.001**
	HSPDP-BTB13-1A	Baringo-Tugen Hills-Barsemoi Basin	This study	3.288–2.577	*δ^2H_{C31} (‰ VSMOW)*	DSDP 231-IODP U1463	TEX_{86}	Liddy et al. (2016) and Smith and Castañeda (2020)	0.21	<0.5		
						ODP 709C-ODP 758	*$\delta^{18}O_p$*	Chen et al. (1995), Farrell and Janecek (1991), Karas et al. (2011), and Shackleton and Hall (1990)	**0.69**	**<0.001**		
						ODP 709C-ODP 763	*$\delta^{18}O_p$*	Karas et al. (2011) and Shackleton and Hall (1990)	0.34	<0.5		
						IODP U1478-IODP U1463	TEX_{86}	Smith and Castañeda (2020) and Taylor et al. (2021)	**0.68**	**<0.005**		
						ODP 709C-ODP 763	Mg/Ca	Karas et al. (2011)	−0.02	<1		

Note. Correlations (r) between hydroclimate proxy data and $\Delta SST_{W\text{-}E}$ and/or SST are bolded if the correlation is significant at or above the 95% confidence range ($p < 0.05$). Certain hydroclimate records and $\delta^{18}O_p$ values (italicized) were inverted so that a positive r always denotes a positive moisture-$\Delta SST_{W\text{-}E}$ relationship.

The relative importance of high and low latitude forcings to the orbital-scale pacing of the eastern African monsoon is also uncertain. Mediterranean sapropels (Emeis et al., 2000; Hilgen, 1991; Lourens et al., 1996; Rose et al., 2016; Rossignol-Strick, 1983, 1985) and alkenone fluxes (Herbert et al., 2015), some northern African dust flux records (Skonieczny et al., 2019), and other eastern African indices of hydroclimate (Caley et al., 2018; Foerster et al., 2022; Joordens et al., 2011; Lupien et al., 2018, 2022; Nutz et al., 2017; Partridge et al., 1997) and vegetation (Lupien et al., 2018, 2021; Yost et al., 2021) suggest that low-latitude seasonal insolation, mainly paced by precession (19–23 kyr), exerts an outsized influence on hydroclimate. However, other dust time series (deMenocal, 1995, 2004; Larrasoaña et al., 2003; Tiedemann et al., 1994; Trauth et al., 2009) and elemental X-ray fluorescence (XRF) ratios (Crocker et al., 2022) contain a strong 41-kyr (obliquity) signal. Obliquity in low-latitude records is traditionally thought to derive from polar ice sheets and their influence on global atmospheric circulation (deMenocal, 2004; Trauth et al., 2009), but the interhemispheric 21 June insolation gradient in the tropics (23.5°N–23.5°S) also has a prominent 41 kyr component. A higher cross-equatorial gradient invigorates the winter Hadley cell, enhancing moisture transport into the summer hemisphere (Bosmans et al., 2015; Mantsis et al., 2014); obliquity controls the Earth's tilt and therefore this gradient, and may explain the 41 kyr cycles in Pliocene African (Kuechler et al., 2018) and Australian (Auer et al., 2019; Christensen et al., 2017; Taylor et al., 2021) and later Pleistocene (O'Mara et al., 2022) hydroclimate records before and after the "41 kyr world" of ∼2.75–0.8 Ma (Lisiecki & Raymo, 2007). A link between ice volume and rainfall is suggested by the eastern-central portions of Africa that were drier during the Last Glacial Maximum (LGM) than today despite similar orbital geometries (Garelick et al., 2021; Gasse, 2000; Otto-Bliesner et al., 2014), yet this teleconnection is spatially variable and may have developed recently (within the last 100 ka) (Lupien et al., 2022).

Indian Ocean (IO) sea surface temperatures (SSTs) and zonal SST gradients are known to play a critical role in interannual to decadal variability of African rainfall (Abram et al., 2008; Saji et al., 1999; Ummenhofer et al., 2009; Webster et al., 1999), but their longer-term influence is poorly known. During large modern positive IO Zonal Dipole (IOZD) events, an anomaly of 3°C in the west-east SST difference ($\Delta SST_{W\text{-}E}$) can cause eastern African flooding and western Indonesian drought (Abram et al., 2008). $\Delta SST_{W\text{-}E}$ has been shown to modulate eastern African and western Indo-Australian precipitation amounts and isotopic composition on seasonal (Saji et al., 1999; Ummenhofer et al., 2009; Vuille et al., 2005; Webster et al., 1999) to multidecadal (Abram et al., 2008, 2020; Tierney et al., 2013) timescales, and is also thought to drive millennial (Konecky et al., 2014; Tierney et al., 2011) and glacial-interglacial (Di Nezio et al., 2016) changes, but the long-term rainfall–IO SST relationship has only been examined on a site-by-site basis and not beyond the late Pleistocene. The influence of the El Niño-Southern Oscillation (ENSO) and the Pacific Ocean has also been invoked to explain long-term changes in eastern African rainfall (de Oliveira et al., 2018; Kaboth-Bahr et al., 2021; Kaboth-Bahr & Mudelsee, 2022; Pausata et al., 2017), although climate models suggest the IO SST gradient exerts a more direct influence (Goddard & Graham, 1999; Latif et al., 1999). Processes that alter IO $\Delta SST_{W\text{-}E}$ on geologic timescales include the northwards movement of New Guinea-Australia and growth of Halmahera in the Pliocene, constricting the Indonesian Throughflow (ITF) and therefore Pacific-eastern IO exchange (Cane & Molnar, 2001; Jochum et al., 2009; Rodgers et al., 2000; Sarnthein et al., 2018), and the meridional migration of the Antarctic subtropical front (STF), which can weaken Agulhas leakage as it approaches South Africa (Bard & Rickaby, 2009; Caley et al., 2012), thereby trapping heat in and warming the western IO (Civel-Mazens et al., 2021).

An improved understanding of terrestrial eastern African hydroclimate could reveal the underlying forcings of African rainfall variability, improve climate prediction, and illuminate drivers of early hominin evolution (Campisano et al., 2017). The Hominin Sites and Paleolakes Drilling Project (HSPDP) recovered a ∼228 m sediment drill core from the Baringo-Tugen Hills-Barsemoi (BTB) Basin, HSPDP-BTB13-1A (hereafter BTB13), which spans ∼3.3–2.6 Ma (Campisano et al., 2017; Cohen et al., 2016). This interval includes iNHG and heightened 41 kyr cyclicity in benthic $\delta^{18}O$ values, several pulses of large lakes in eastern Africa (Trauth et al., 2005, 2007), and evolutionary innovations associated with *Australopithecus* and *Homo* lineages (deMenocal, 2004; Maslin et al., 2014; Shultz et al., 2012). At the basin scale, sedimentological and ecological indicators in BTB13 suggest that some aspects of late Pliocene environmental variations were paced by orbital precession (Deino et al., 2006, 2021; Kingston et al., 2007; Lupien et al., 2022; Yost et al., 2021), but a long, continuous paleoprecipitation record is still lacking.

In sum, the relative influences of precession (local seasonal insolation) versus obliquity (ice volume, the cross-equatorial insolation gradient) and IO $\Delta SST_{W\text{-}E}$ in the late Pliocene—and the extent to which their evolution across iNHG—influenced African climate are still largely unknown and difficult to resolve without high resolution

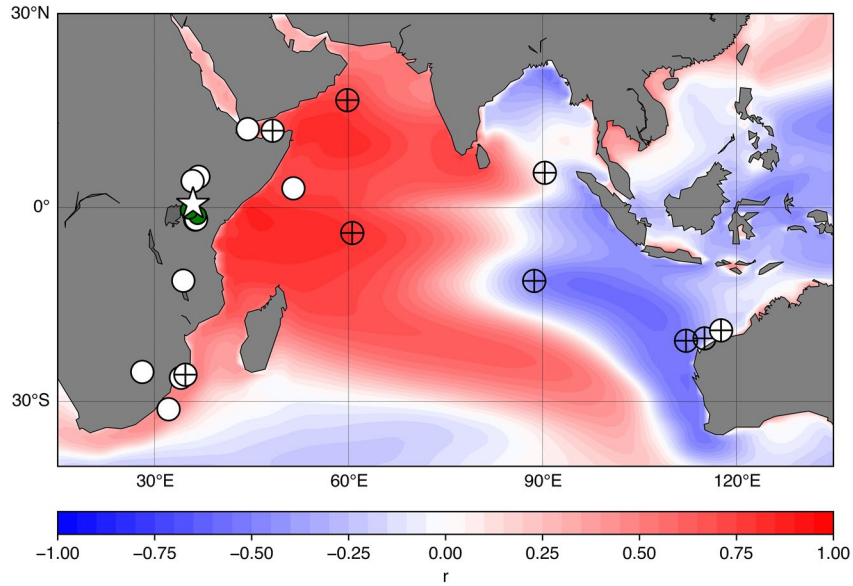

Figure 1. Locations of Kenyan Global Network of Isotopes in Precipitation stations (green), HSPDP-BTB13-1A (white star), and other Pliocene-Holocene terrestrial hydroclimate (white circle) and sea surface temperature (SST) records (cross). Background is annual field correlations (r) between an 1,800-year preindustrial control run of CESM1 SSTs and mean annual eastern African rainfall (averaged over −5.183–7.068°N and 35–46.25°E) (Tierney et al., 2013). See Table 1 and Figure 4 for site names.

paleohydrological data. To address these issues, suborbitally resolved leaf wax *n*-alkane compound-specific hydrogen isotope (δ^2H_{wax}) data from the Baringo Basin are used here to reconstruct rainfall variations in equatorial Kenya across the Plio-Pleistocene boundary. We examine changes in both secular trend and cyclicity of our record to evaluate the importance of global temperature and high-latitude glaciation versus local seasonal insolation. We also compare eastern African and western Australian paleohydroclimate data to $\Delta SST_{W\text{-}E}$ over the last ∼3.5 Ma to assess the strength of IO Walker circulation over the Plio-Pleistocene. Given that IO $\Delta SST_{W\text{-}E}$ is projected to shift toward a mean positive IOZD state in the near future (Abram et al., 2008; An et al., 2022; Cai et al., 2009, 2013, 2014), intensifying the eastern African "monsoon" (Ogega et al., 2020; Shongwe et al., 2011), it is imperative that we improve our predictions of IO SSTs and $\Delta SST_{W\text{-}E}$ and their mechanistic links with rainfall in the twenty-first century and beyond.

1.1. Climatic-Geologic Setting

BTB is an isolated lacustrine basin in the central Kenyan eastern African Rift System that hosts the present-day Lake Baringo (Figure 1). The BTB13 site (0.5546°N, 35.9375°E) is located approximately 10 km southwest of the lake and 10 km east of the Tugen Hills. Seasonal rainfall is primarily controlled by the meridional transit of the Intertropical Convergence Zone (ITCZ), with rainfall maxima coincident with biannual temperature maxima in October–December ("short rains") and March–May ("long rains") when the ITCZ crosses the equator (Herrmann & Mohr, 2011). Precipitation variability is also correlated with IO $\Delta SST_{W\text{-}E}$ and ENSO (Abram et al., 2020), although the IOZD more directly regulates rainfall than ENSO due to nonlinearities in the IOZD-ENSO relationship (Nicholson, 1997; Nicholson & Kim, 1997). During a positive IOD event, warmer-than-average SSTs develop in the western IO, and the ascending eastern African and descending Indo-Australian branches of the Walker Circulation result in increased African and reduced Indo-Australian rainfall (Abram et al., 2008; Saji et al., 1999; Webster et al., 1999). Conversely, during a negative IOZD, when the eastern IO is warmer, the Maritime Continent gets wetter and eastern Africa dries.

The modern-day isotopic composition of central Kenyan rainfall is anticorrelated with precipitation amount on seasonal timescales (Figure 3). Kenya has two Global Network of Isotopes in Precipitation (GNIP) stations with meteoric δ^2H (δ^2H_{H2O}) data (IAEA/WMO, 2023); rainfall amount (mm) and δ^2H_{H2O} values (‰ VSMOW) are negatively correlated year-round at Muguga ($r = -0.64$, $p < 0.05$) and winter-summer at Kericho (January–

August $r = -0.80$, $p < 0.05$; year-round $r = -0.17$, $p < 1$) (Figure 3). Mean annual eastern African rainfall is also positively correlated with a large IO $\Delta SST_{W\text{-}E}$ (Tierney et al., 2013) and ^{18}O- or deuterium-depletion (Konecky et al., 2014; Vuille et al., 2005).

1.2. Orbital Forcing of Eastern African Hydroclimate

Although long, high-resolution terrestrial hydroclimate records spanning the Plio-Pleistocene boundary from the IO rim are sparse, those that exist—IODP Site U1478 δ^2H_{C28} values (Taylor et al., 2021) and International Ocean Drilling Program (IODP) Site U1463 K % (Auer et al., 2019; Christensen et al., 2017)—are paced most strongly by obliquity and eccentricity. In the mid- to later Pleistocene, however, many younger eastern African records have a strong 19–23-kyr precessional imprint (Caley et al., 2018; Foerster et al., 2022; Lupien et al., 2018, 2022; Partridge et al., 1997; Simon et al., 2015). This suggests a complex set of high- and low-latitude African and IO climate forcings (e.g., deMenocal, 1995, 2004).

1.3. Prior Work on HSPDP-BTB13-1A

The studied interval lies within the Chemeron Formation (5.3–1.6 Ma) (Chapman & Brook, 1978; Deino & Hill, 2002; Hill et al., 1986), which consists of a mix of fluviolacustrine sands, clays, silt, conglomerate, and volcanic ash. The Bayesian age model of BTB13 is based on $^{40}Ar/^{39}Ar$ dating of tuffaceous layers, correlations of diatomite contacts in the core with those in nearby outcrop (Deino et al., 2021), trace-element tephrostratigraphy (Garello, 2019), and magnetostratigraphy (Sier et al., 2021). In the top 55 m (~2.68–2.55 Ma), the model's 95% confidence interval is under ±20 kyr. From 55 m to core bottom, the 95% confidence interval can range up to ±60 kyr. However, individual control point errors range from 3 to 87 kyr, averaging 14 kyr ($\pm 1\sigma$), and despite Bayesian uncertainty envelopes, control points suggest highly linear sedimentation rates (on $>10^1$ kyr timescales) within the 2.75–2.58, 2.93–2.75, and 3.28–2.93 Ma windows (Figure 2a).

Prior sedimentologic and micropaleontologic work on BTB13 and nearby outcrops suggest that the Baringo Basin experienced semi-wet, fluviolacustrine-alluvial-deltaic conditions prior to ~3.04 Ma. Afterward, the environment alternated between shallow, marshy lakes and C_4 grasslands and deeper lakes and C_3 grasslands (Westover et al., 2021). Based on paleoecological proxies such as biomarker $\delta^{13}C_{C28}$ values (Lupien et al., 2019) and phytolith ratios (Yost et al., 2021), C_4 grasses increased relative to forest by 3.05–3 Ma. Ichthyolites (Billingsley et al., 2021) and diatomite strata (Westover et al., 2021) increase in abundance between 3.04 and 2.95, indicating lake highstands favorable to diatoms and fish; diatom assemblages (Kingston et al., 2007; Westover et al., 2021) and fish fossil $\delta^{13}C$ values (Billingsley et al., 2021) are both characteristic of deep lacustrine environments. Alternating diatomites and analcime-bearing sedimentary strata diagnostic of alkaline, highly-evaporated brines imply repeated and abrupt wet-dry transitions from 2.99 Ma onwards (Minkara, 2017). The youngest set of BTB13 diatomites observed in the core and exposed nearby (D_8–D_4 (Westover et al., 2021)) correspond to 23-kyr-paced 30°N 21 June insolation maxima from ~2.68 to 2.58 Ma (Deino et al., 2006).

The Baringo Basin thus documents pronounced environmental change, including apparent incongruous hydroclimatic shifts (e.g., more frequent lake highstands alongside grassland expansion). Thus far it has been difficult to conclusively disentangle climatic and tectonic influences on the existing proxy records, particularly on >100 kyr timescales. Phytolith indices (Yost et al., 2021) and the pacing of diatomites D_8–D_4 (Deino et al., 2006; Kingston et al., 2007) suggest that precipitation variability was at least partially forced by orbital precession; however, the absence of highstands (i.e., diatomites) during precessional insolation maxima prior to 3.05 Ma remains unexplained.

2. Materials and Methods

2.1. Core Scanning X-Ray Fluorescence and Magnetic Susceptibility

A Geotek MSCL-XYZ multisensor core logger was used to measure magnetic susceptibility (MS) at 0.5 cm intervals. MS varies with the relative amount of magnetic minerals and therefore the relative proportions of weakly- or nonmagnetic biogenic silica, carbonates, and organic matter versus iron-rich detrital sediment (Hounslow & Maher, 1999; Verosub & Roberts, 1995). It is commonly employed as an indicator of weathering or runoff (Bloemendal & deMenocal, 1989; Larrasoaña et al., 2008).

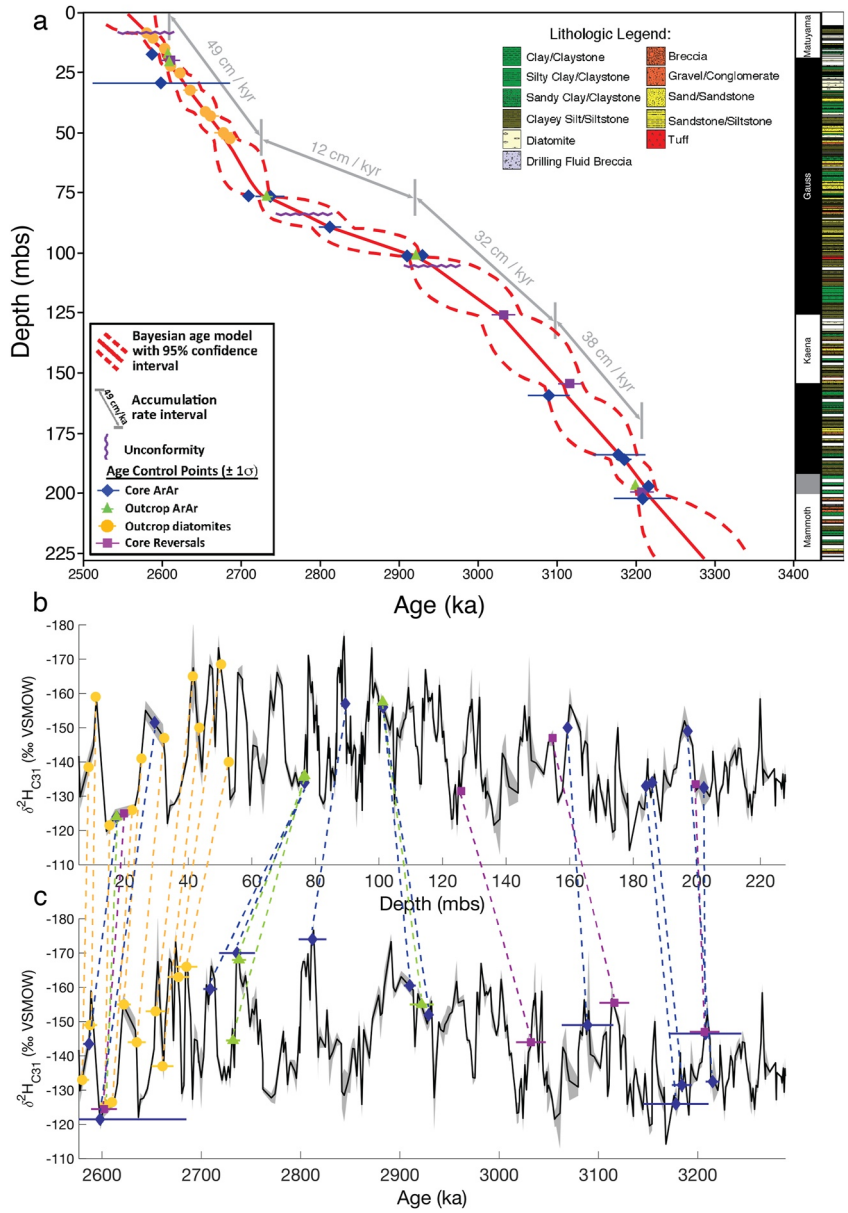

Figure 2. (a) Bayesian age model and lithologies of HSPDP-BTB13-1A (BTB13) (Deino et al., 2021). BTB13 δ^2H_{C31} values plotted against (b) depth and (c) age, with horizontal lines indicating $\pm 1\sigma$ of age control points and gray shading indicating analytical δ^2H $\pm 1\sigma$. Dashed lines denote the same control points in depth/age space.

Continuous XRF scanning yielded estimates of elemental concentrations in BTB13. Si/Ti is a proxy for biogenic silica concentrations (Brown, 2015; Johnson et al., 2011; Westover et al., 2021), that is, diatom abundance, and therefore lake depth and productivity. These data provide the highest-resolution measurements available from BTB13 and can be used to test if local basin-scale responses result from changes in atmospheric circulation suggested by our δ^2H_{wax} measurements.

2.2. Leaf Wax Biomarkers

Plant epicuticular waxes protect leaves from dehydration and damage and are resistant to diagenesis on geologic timescales (T. I. Eglinton & Eglinton, 2008; Sessions et al., 2004). Since environmental (soil, rain-) water is the primary hydrogen source for photoautotrophic biosynthesis, the hydrogen isotopic composition of plant epicuticular lipids (δ^2H_{wax}) correlates strongly with δ^2H_{H2O} values (Sachse et al., 2012). Long-chain *n*-alkanes derive

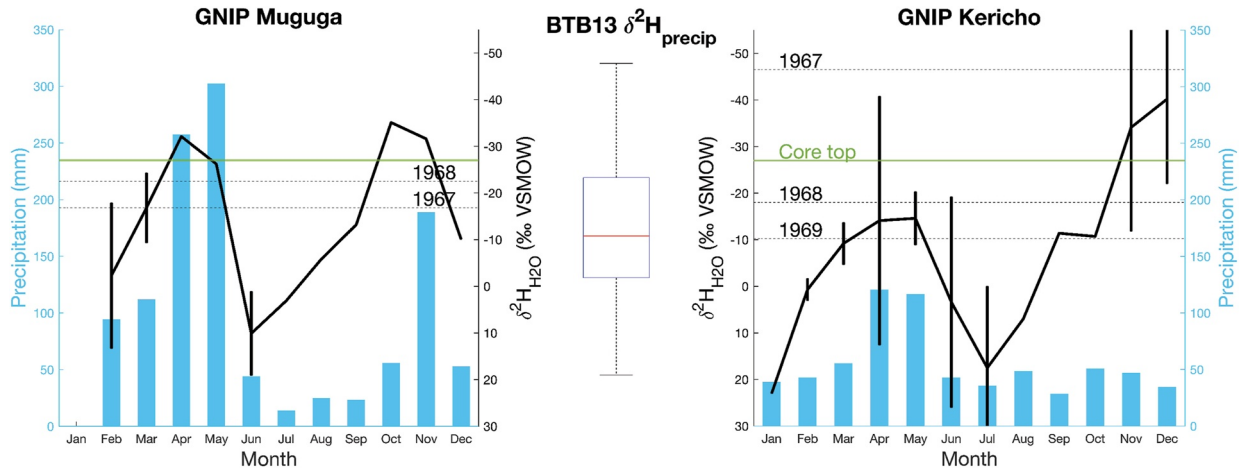

Figure 3. Mid-twentieth century monthly mean precipitation amounts and δ^2H_{H2O} values from Kenyan Global Network of Isotopes in Precipitation stations with annual weighted mean δ^2H_{H2O} values from 1967 to 1969 (dashed lines), a core-top (i.e., modern day) δ^2H_{precip} reconstruction from modern-day Lake Baringo (Bessems et al., 2008) (green line), and a box and whisker plot of reconstructed Plio-Pleistocene HSPDP-BTB13-1A δ^2H_{precip} values. Vertical black lines denote interannual δ^2H_{H2O} variance.

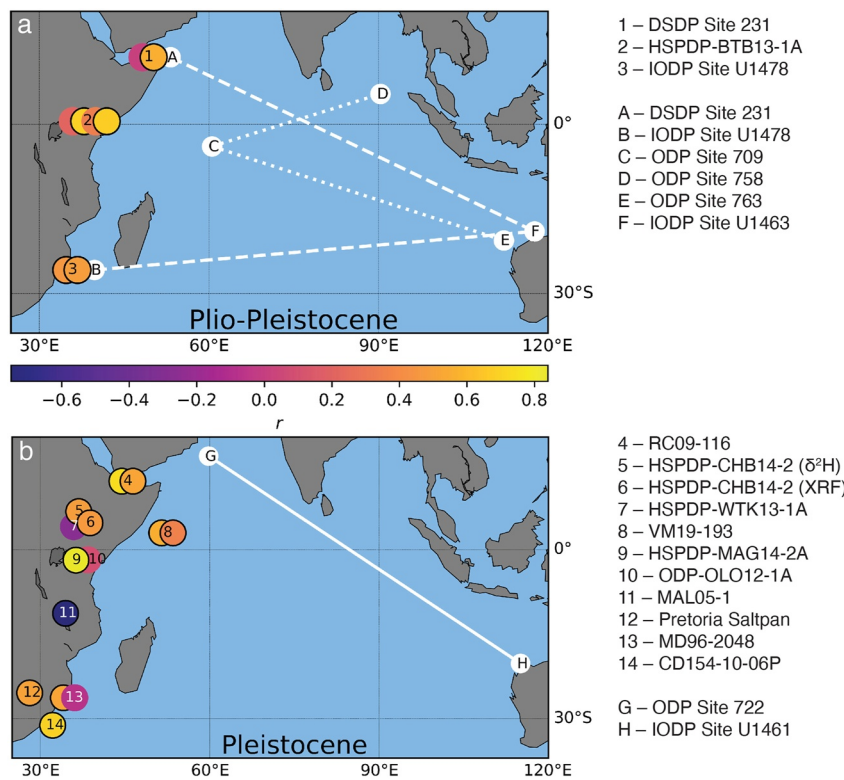

Figure 4. Correlations (r) between (a) Plio-Pleistocene and (b) Pleistocene-Holocene hydroclimate proxy data and $\Delta SST_{W\text{-}E}$. If symbols are outlined, the correlation is significant at or above the 95% confidence range ($p \leq 0.05$). Certain hydroclimate records and $\delta^{18}O_p$ values were inverted so that a positive r always denotes a positive moisture-$\Delta SST_{W\text{-}E}$ relationship. The line style used for sea surface temperature (SST) transects denotes the type of proxy used (dashed = TEX_{86}; dotted = $\delta^{18}O_p$ values; solid = $U^{k'}_{37}$). (See Table 1 for references.) Terrestrial sites compared with more than one SST transect/paired SST measurements have multiple symbols.

primarily from higher-order terrestrial plants and grasses (Sachse et al., 2012), and so their δ^2H_{wax} values track meteoric rather than lacustrine δ^2H_{H2O} values. Although δ^2H_{H2O} values are subject to fractionation by altitude, temperature, etc., in the tropics they are largely a function of precipitation amount and the progressive Rayleigh fractionation that depletes rainwater of deuterium (Dansgaard, 1964; Rozanski et al., 2013). Because δ^2H_{H2O} values are determined by broader atmospheric processes, δ^2H_{wax} values reflect regional (10^2–10^3 km^2) hydroclimate variations and are therefore relatively insensitive to changes in basin-scale (<10 km^2) geomorphology. Thus, here, we report *n*-alkane δ^2H_{wax} values as an indicator of equatorial eastern African hydroclimate.

A Thermo Fisher (Dionex) Accelerated Solvent Extractor 350 (solvent: 9:1 dichloromethane: methanol) was used to extract lipids from freeze-dried, homogenized sediment. *N*-alkanes were purified from the total lipid extract by sequential flash aminopropyl (60 Å), silica gel (230–400 mesh), and silver nitrate-impregnated silica gel (~10 weight percent, +230 mesh) column chromatography. Alkane abundances were measured on Agilent 6890 and 7890 gas chromatography (GC)-flame ionization detectors with Agilent HP-1 MS columns (30 m × 0.25 mm × 0.25 μm) and quantified using the TEXPRESS MATLAB package (Dillon & Huang, 2015).

We obtained C_{31} and C_{33} *n*-alkane δ^2H (δ^2H_{C31}, δ^2H_{C33}) and $\delta^{13}C$ values ($\delta^{13}C_{C31}$, $\delta^{13}C_{C33}$) using an Agilent 6890 GC equipped with an RTX-5 MS column (30 m × 0.32 mm × 0.25 μm) coupled to a Thermo Delta V Plus isotope ratio mass spectrometer whose pyrolysis (hydrogen)/combustion (carbon) reactor was held at 1,410–1,425°C (hydrogen) or 1,100°C (carbon). The oven program was: hold for 2 min at 50°C, increase to 230°C at 15°C/min, increase to 320°C at 4°C/min, hold for 8 min. H_3^+ factors (Sessions et al., 2001), measured at least every 3 days, averaged 2.00 ± 0.05 (1σ). A mixture of *n*-alkane standards ($\delta^2H_{C29} = -162.6 \pm 2.2‰$; $\delta^2H_{C31} = -271.9 \pm 2.0‰$; $\delta^2H_{C32} = -212.4 \pm 1.0‰$; $\delta^{13}C_{C29} = -29.30 \pm 0.02‰$; $\delta^{13}C_{C31} = -29.43 \pm 0.01‰$; $\delta^{13}C_{C32} = -29.47 \pm 0.02‰$) from Arndt Schimmelmann (Indiana University) was injected before every δ^2H or every other $\delta^{13}C$ measurement. The mean difference between bracketing measured and reported C_{29}–C_{32} δ^2H values was applied to measured δ^2H_{C31} and δ^2H_{C33} values to correct for instrument offset and drift. Reported values (Figures 4 and 5) are the average of multiple individual measurements and reported error values are ±1σ if a sample was replicated ≥3 times; the difference between duplicate δ^2H or $\delta^{13}C$ values if measured twice; and the difference between bracketing Indiana δ^2H_{C31} or $\delta^{13}C_{C31}$ values if injected once.

We measured δ^2H_{C31} values in 298 samples to create a ~2.4-kyr resolution record in order to characterize the shortest Milankovitch cycles (19, 23 kyr). We also measured leaf wax isotopes in recent (<0.2 ka) sediments from Lake Baringo (Bessems et al., 2008) as a modern-day baseline (Figure 3). Hereafter, we focus on the paleohydrology of eastern Africa via BTB13 δ^2H_{wax} values; the paleoecological implications of the $\delta^{13}C_{wax}$ data will be discussed in a future publication and are only used here to reconstruct the hydrogen isotopic composition of rainwater (δ^2H_{precip}).

2.3. δ^2H_{precip} Calculations

δ^2H_{precip} values can be estimated using δ^2H_{wax} and $\delta^{13}C_{wax}$ values (Collins et al., 2013). Here, we use them as a first-order constraint on the magnitude of hydrologic change implied by the δ^2H_{C31} record by comparing them to modern δ^2H_{H2O} values (Figure 3), but since the δ^2H_{C31} data are higher-resolution ($n = 298$) than δ^2H_{precip} ($n = 200$), all analyses will be performed using δ^2H_{C31} values.

Water-wax fractionation ($\varepsilon_{wax\text{-}H2O}$) differs by plant species and can be estimated from $\delta^{13}C_{wax}$ measurements; using 100% tropical C_3 and C_4 $\delta^{13}C_{C31}$ endmembers of −36.7 ± 3.2‰ and −22.0 ± 2.6‰ (Ruan et al., 2019), respectively, $\delta^{13}C_{wax}$ values provide the relative abundance of C_3 (fC_3) and C_4 (fC_4) plants in terrestrial vegetation surrounding BTB via a linear mixing model (e.g., Garelick et al., 2021; Konecky et al., 2016; Lupien et al., 2022; Shanahan et al., 2015):

$$fC_3 = \left(\delta^{13}C_{C31} - \delta^{13}C_{C31\,C4}\right) / \left(\delta^{13}C_{C31\,C3} - \delta^{13}C_{C31\,C4}\right)$$

$$fC_4 = 1 - fC_3$$

A tropical (30°N–30°S) subset of δ^2H_{wax} and $\delta^{13}C_{wax}$ values in modern vegetation yields an average apparent $\varepsilon_{C31\text{-}H2O}$ of C_3 and C_4 plants—$\varepsilon_{C31\text{-}precip\ C3}$ and $\varepsilon_{C31\text{-}precip\ C4}$—of −123 ± 40 and −136 ± 28‰, respectively (Ruan et al., 2019). Thus,

$$\varepsilon_{C31\text{-}H2O} = \left(fC_3 * \varepsilon_{C31\text{-}precip\,C3}\right) + \left(fC_4 * \varepsilon_{C31\text{-}precip\,C4}\right)$$

and

$$\delta^2H_{precip} = \left[\left(\delta^2H_{C31} + 1000\right) / \left(\varepsilon_{C31\text{-}H2O}/1000 + 1\right)\right] - 1000$$

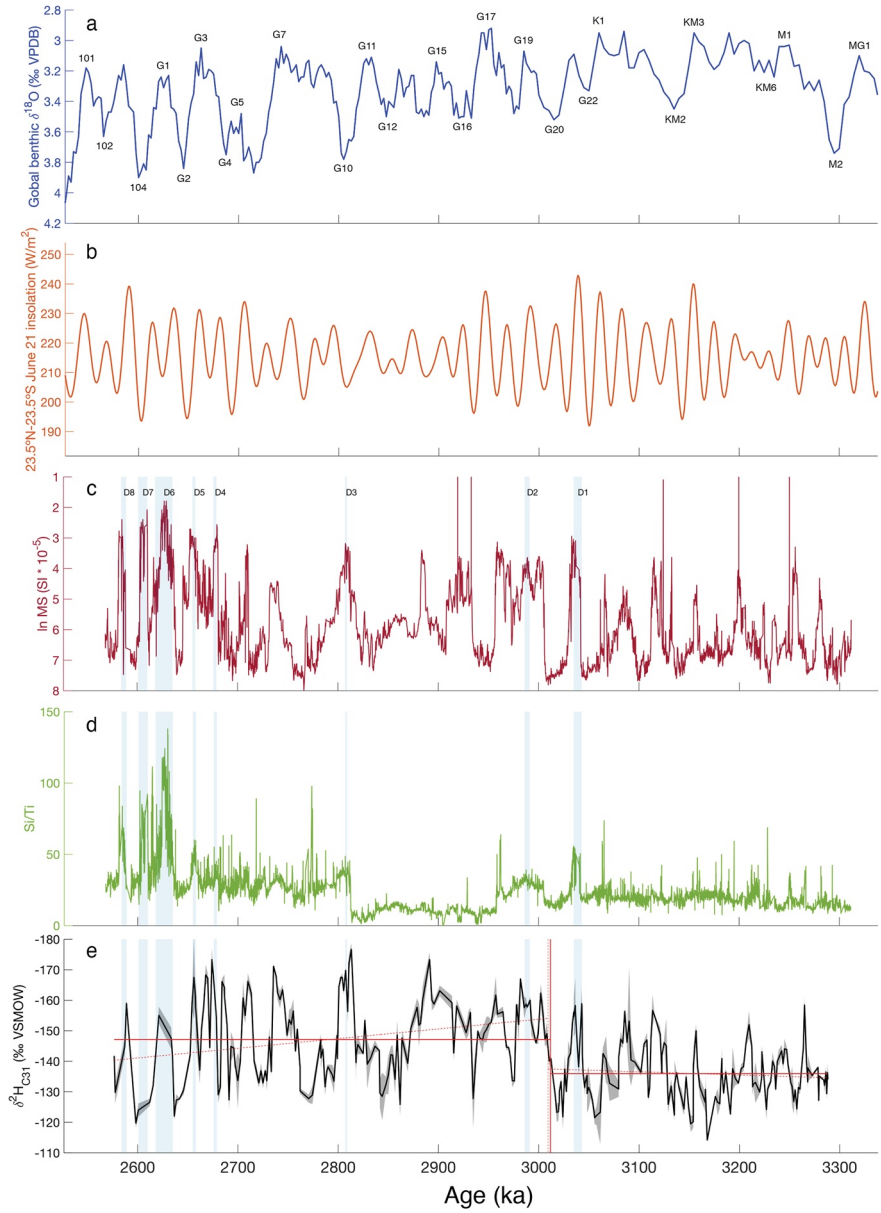

Figure 5. Global and local eastern African climate parameters, including (a) the LR04 benthic foraminiferal $\delta^{18}O$ stack (Lisiecki & Raymo, 2005); (b) 21 June 23.5°N–23.5°S insolation gradient (black); (c) BTB13 ln magnetic susceptibility, with blue bars denoting significant diatomite strata D_1–D_8 (Westover et al., 2021); (d) BTB13 X-ray fluorescence Si/Ti; and (e) BTB13 δ^2H_{C31} values. Vertical solid red line shows the timing of the single most abrupt shift in mean. Solid horizontal red lines show mean values before and after the changepoint. Vertical dashed red line shows the timing of the single most abrupt shift in slope and horizontal dashed red lines show the trend in δ^2H_{C31} values before and after. Gray shaded intervals indicate analytical error ($\pm 1\sigma$).

2.4. Plio-Pleistocene Terrestrial Hydroclimate and Indian Ocean Temperature Data Compilation

To evaluate the climatic controls on Plio-Pleistocene eastern African hydroclimate, we analyze long-term (>100 kyr timescales) variations in our data relative to other long records from across the IO basin (Table 1). Vegetation data sets (Castañeda et al., 2016; Feakins et al., 2005) are excluded, as African plant assemblages may depend on other factors than rainfall such as pCO_2 (Crocker et al., 2022; O'Mara et al., 2022; Polissar et al., 2019). We exclude records shorter than 200 kyr for reasons explained below.

Plio-Pleistocene hydroclimate data include δ^2H_{wax} data from the Baringo Basin, IODP Site U1478 (Taylor et al., 2021), and Deep Sea Drilling Project (DSDP) Site 231 (Liddy et al., 2016). To increase geographical and

temporal coverage, we also analyzed hydrological proxy (δ^2H_{wax} and elemental XRF) records from the Pleistocene (2.1–0 Ma) (Caley et al., 2018; Foerster et al., 2022; Johnson et al., 2016; Lupien et al., 2018, 2022; Owen et al., 2018; Partridge et al., 1997; Potts et al., 2020; Simon et al., 2015; Tierney et al., 2017). In the present, drought in Australia coincides with heavy rains in eastern Africa during a positive IOZD event. We used natural gamma radiation (NGR) K % (Auer et al., 2020; Christensen et al., 2017), which reflects detrital sedimentation generally, and the XRF (K + Al)/Ca ratio (Auer et al., 2019), which is more specifically controlled by riverine influx, from western Australian IODP Site U1463 to test this teleconnection across the Plio-Pleistocene boundary (Figures 1 and 6).

IO SST data were selected from locations where preindustrial-modern SSTs and eastern African precipitation are strongly correlated (Tierney et al., 2013) (Figure 1). For this reason, we exclude central IO DSDP Site 214 whose Mg/Ca SSTs are intermediate between western and eastern values (Karas et al., 2009). We construct five late Pliocene IO $\Delta SST_{W\text{-}E}$ transects from existing SST records based on comparisons between the same temperature proxies (Table 1; Figure 4a). To mitigate proxy biases related to seasonality, formation depth, etc. (Tierney & Tingley, 2015), we avoid mixing and matching TEX_{86} or Mg/Ca temperatures or planktic foraminiferal $\delta^{18}O$ ($\delta^{18}O_p$) values. While $\delta^{18}O_p$ values are responsive to both temperature and ice volume, multi-proxy SST reconstructions suggest that TEX_{86} and $\delta^{18}O_p$ trends are relatively interchangeable (De Vleeschouwer et al., 2022; Smith & Castañeda, 2020), independently confirmed by Δ_{47} measurements (De Vleeschouwer et al., 2022). In the Pleistocene, long SST records are sparse; only one proxy-consistent ($U^{k'}_{37}$) zonal transect can be constructed that spans 2.5–0 Ma (Table 1; Figure 4b).

We also use existing paleo-data sets to discern the relative influences of potential high northern and southern latitude processes on eastern African hydroclimate and IO $\Delta SST_{W\text{-}E}$. Extensive SST (Clotten et al., 2018; Lawrence et al., 2009; Naafs et al., 2020), ice-rafted debris (IRD) (Bailey et al., 2013), and foraminiferal $\delta^{18}O$ data (Bartoli et al., 2005; Kleiven et al., 2002; Lisiecki & Raymo, 2005) exist from the Arctic/North Atlantic. We use the correlation between southwest IO SSTs, which reflect the strength of the IO-side Agulhas current (Taylor et al., 2021), and southern Atlantic SSTs, which track the meridional migration of the STF (Martínez-Garcia et al., 2010), to evaluate the effects of Antarctic cooling on IO temperatures. If these are anticorrelated—i.e., if the Mozambique Channel warms when the STF moves north—it might indicate that this teleconnection was active in the Pliocene and influencing $\Delta SST_{W\text{-}E}$. We interpolated these two SST records to the same evenly spaced ∼9-kyr resolution and performed a running 10-point linear regression of Site 1090 ($U^{k'}_{37}$) and U1478 (TEX_{86}) SSTs; the Pearson's *r* is shown in Figure 8. This involves the comparison of disparate proxies, but is unavoidable due to the dearth of Pliocene Southern Atlantic/IO SST records.

2.5. Spectral Analyses and Resampling Methods

Due to variable resolution, comparing $\Delta SST_{W\text{-}E}$ to terrestrial hydroclimate requires multiple resampling steps. Ultra-high-resolution (<0.1 kyr) XRF data (CD154-10-06P, MAL05-1, HSPDP-CHB14-2, ODP-OLO12-1A) were interpolated to a common 0.5 kyr step. For every $\Delta SST_{W\text{-}E}$-hydroclimate pair, we calculated the mean resolutions of the two SST data sets over the timespan that they overlapped with the hydroclimate proxy record and interpolated the SST data sets to the lower of the two resolutions. Age model uncertainties could bias the short-term correlation between precipitation and $\Delta SST_{W\text{-}E}$, so we focus on long-term relationships by using a low-pass sixth order Butterworth filter on both $\Delta SST_{W\text{-}E}$ and the hydroclimate proxy and exclude short (<200 kyr) data sets (e.g., Cohen et al., 2007; Ziegler et al., 2013). Given age model uncertainty (up to ∼40 kyr) and the low resolution of $\Delta SST_{W\text{-}E}$ (>40 kyr) in certain areas/times, we opted to only examine long term variance. For <250 kyr records, the low-pass filter removed <100 kyr trends; for longer data sets, it removed <200 kyr frequencies. Finally, we interpolated low-pass filtered $\Delta SST_{W\text{-}E}$ and hydroclimate data to the same 20 evenly sampled points to calculate the correlation coefficient (Pearson's *r*) of a linear regression of the two. For IODP Site U1478 and DSDP Site 231, where δ^2H_{wax} values and TEX_{86} were measured on the same samples, we calculated *r* among δ^2H_{wax} values and SSTs without any interpolation. We performed a similar comparison between hydroclimate (XRF Fe/Ca) and SSTs (the first principal component [PC1] of Mg/Ca and foraminiferal assemblages) in the Pleistocene MD96-2048 core, but this additionally required interpolation to the mean resolution of the SST PC1.

The values for some hydroclimate and SST proxies are inversely related to precipitation amount and temperature, so all isotope (δ^2H_{wax}, $\delta^{18}O_p$ values) and certain XRF data sets (K/Zr, Na/Ca, Ca) were multiplied by −1 prior to calculating *r* such that a positive *r* always indicates a positive eastern African moisture-$\Delta SST_{W\text{-}E}$ relationship (Table 1; Figure 4).

10.1029/2023PA004671

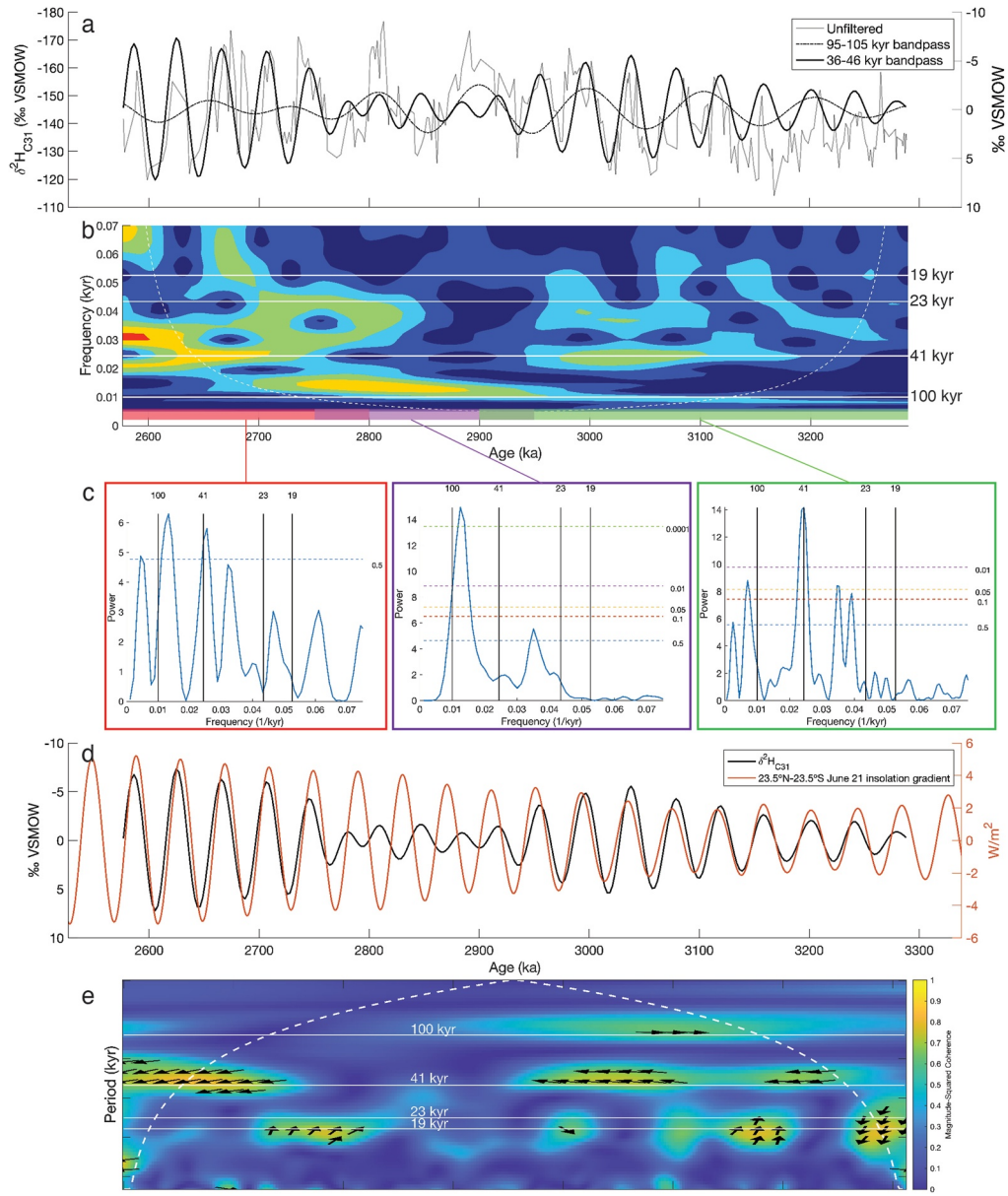

Figure 6. Spectral characteristics of the BTB13 δ^2H_{C31} record. (a) Unfiltered (gray) and 36–46 kyr (black) and 95–105 kyr (dash-dotted) bandpass filtered δ^2H_{C31} values. (b) δ^2H_{C31} evolutionary wavelet power spectrum. Dashed white line denotes cone of influence. (c) Lomb-Scargle power spectra of 2.80–2.58 Ma (red), 2.95–2.75 (purple), and 3.28–2.90 Ma (green) intervals. Dashed lines denote false alarm probability. (d) 36–46 kyr-bandpass filtered δ^2H_{C31} values (black) and 21 June 23.5°N–23.5°S insolation gradient (orange). (e) Wavelet cross-spectrum of BTB13 δ^2H_{C31} values and 21 June 23.5°N–23.5°S insolation gradient. Dashed white line denotes cone of influence. Arrows (≥0.60 magnitude-squared coherence) pointing to the left indicate 0° phase lead/lag.

We pinpoint the most significant secular changes in BTB13 and western Australian hydroclimate records based on the timing of the single largest change in mean and/or slope of the time series via MATLAB's findchangepts function (Killick et al., 2012; Lavielle, 2005). These data were first interpolated to a constant time-step equal to the mean resolution of the original data.

We used multiple methods to characterize the changing strengths of different frequencies of variability in BTB13 hydroclimate records. Lomb-Scargle power spectra detect periodicity in unevenly sampled data sets, but require a minimum sample resolution and therefore do not function during low-resolution periods such as the upper 70 kyr of the δ^2H_{C31} record, while evolutionary Wavelet power spectra require interpolation to a constant timestep

but still work in low-resolution intervals. To ensure that spectral power was not an artifact of upsampling, we confirmed the wavelet results with Lomb-Scargle power spectra. To assess the spectral coherency between two paleoclimate data, we interpolated both to the same timestep—the mean resolution of the lower-resolution record—and performed an evolutionary Wavelet cross-spectral analysis (Trauth, 2021).

3. Results

3.1. HSPDP-BTB13-1A *N*-Alkane δ^2H Values

Biomarker concentrations and therefore sampling resolution were lowest in the uppermost 80 kyr and within diatomites D_8–D_6 in particular (Westover et al., 2021). BTB13 δ^2H_{C31} and δ^2H_{C33} values covary ($r = 0.69$; $p < 0.001$; $n = 298$); C_{31} *n*-alkanes were typically the most abundant, followed by C_{33} and C_{29}. Therefore, only C_{31} isotope data sets are interpreted here. δ^2H_{C31} values average −142.7‰ and range from −176.6 to −114.2‰.

The carbon preference index (CPI) denotes the dominance of odd- over even-carbon alkanes and is used to identify diagenetically degraded hydrocarbons, which typically have CPIs of ∼1 (Bray & Evans, 1961; Bush & McInerney, 2013; G. Eglinton & Hamilton, 1967; Marzi et al., 1993).

$$CPI_{27-35} = [\Sigma_{odd}(C_{27} - C_{33}) + \Sigma_{odd}(C_{29} - C_{35})]/2[\Sigma_{even}(C_{28} - C_{34})]$$

The mean CPI_{27-35} in BTB13 is 3.26 (0.85–7.16; $n = 382$), indicating generally good wax preservation. CPI_{27-35} and δ^2H_{C31} values are weakly but significantly correlated ($r = 0.27$; $p < 0.001$), but none were excluded from analyses on this basis for several reasons. First, CPI_{27-35} variance explains <10% of the variance in the δ^2H_{C31} signal. Second, the depositional environment is unlikely to be deep or warm enough for significant deuterium substitution in alkanes (Leif & Simoneit, 2000; Schimmelmann et al., 2006). Third, oxidative degradation of waxes is expected to be heightened during dry periods such that CPI would be anticorrelated with δ^2H_{C31} values (Pond et al., 2002; Schimmelmann et al., 2006), but this is the opposite to what we observe. Finally, excluding low δ^2H_{C31} data below a CPI value of 3.628, the point at which the CPI_{27-35}-δ^2H_{C31} relationship is insignificant at the 95% confidence level (i.e., $p > 0.05$), does not affect any of the major features of the δ^2H_{C31} record (Figure S1 in Supporting Information S1).

δ^2H_{precip} and δ^2H_{C31} values are highly correlated ($r = 0.99$) and the standard deviation in $\varepsilon_{C31\text{-}H2O}$ is 1.7‰, much smaller than δ^2H variability. The δ^2H_{precip} value (−27.0‰) estimated from Lake Baringo core-top plant waxes (Bessems et al., 2008) approximates twentieth century weighted mean annual δ^2H_{H2O} values at Muguga (−22.5 to −16.8‰) and Kericho (−46.5 to −10.2‰) GNIP stations (Figure 3), indicating that our δ^2H_{precip} methodology plausibly approximates mean annual δ^2H_{H2O} values. The total range in Plio-Pleistocene BTB13 δ^2H_{precip} values (∼60‰) is slightly greater than the mannual range in modern Kenyan δ^2H_{H2O} values (40–50‰).

Seven of eight diatomites are contemporaneous with δ^2H_{C31} minima. (No δ^2H_{C31} measurements were made within D_7.) Change point analysis, confirmed by a running 70-point Mann-Whitney test (Mann & Whitney, 1947) (Figure S2 in Supporting Information S1), indicates a ∼−11.5‰ (Student's *t*-test $p < 0.001$) shift around 3 Ma (Figure 5e), suggesting wetter mean conditions starting at this time. Mean δ^2H_{C31} values appear more enriched from 2.65 to 2.58 Ma, but since this is at the record's edge and is relatively low-resolution, it is difficult to determine if this is a permanent reversion to a drier state.

3.2. Spectral Characteristics of HSPDP-BTB13-1A Data Sets

Evolutionary Lomb-Scargle spectra of both MS and Si/Ti are largely dominated by longer (41-, 100-kyr) frequencies, except for the interval from 2.68 to 2.58 Ma containing precessionally-paced diatomites D_8–D_4 (Figure S3 in Supporting Information S1). Evolutionary wavelet spectra of δ^2H_{C31} values reveal that precession is largely absent; obliquity dominates at the beginning and end of the core (3.2–2.95 and 2.7–2.58 Ma), while 100-kyr variability is strongest in the middle (2.95–2.7 Ma) when 23.5°N–23.5°S summer insolation gradient amplitude is lowest (Figure 6b). Lomb-Scargle periodograms show that the strong obliquity and eccentricity imprints from 3.28 to 2.95 and 2.95 to 2.7 Ma, respectively, are statistically significant ($p < 0.05$); 41 and 100 kyr variability in the last 120 kyr (2.7–2.58 Ma) are not ($p < 0.5$), likely due to low sampling resolution, but the 100 and 41 kyr peaks are still the most prominent (Figure 6c).

The highly linear sedimentation rates in BTB13 (within three large zones) should not strongly impact the results of Wavelet or Lomb-Scargle analyses (Figures 6b and 6c), though the age model imprecision limits phase (lead/lag)

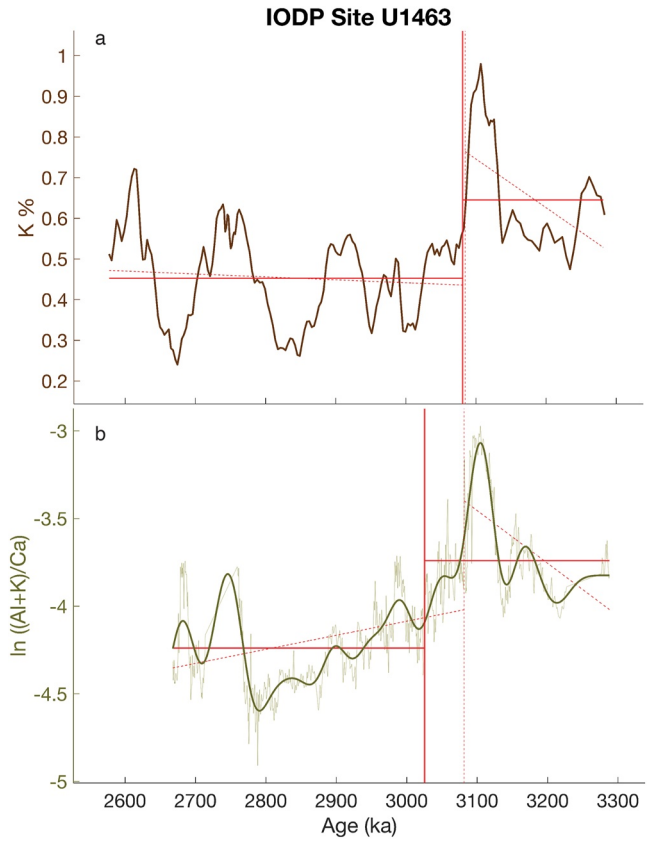

Figure 7. (a) Natural gamma radiation K % and (b) X-ray fluorescence ln ((Al + K)/(Ca)) data from West Australian International Ocean Drilling Program Site U1463 (Auer et al., 2019; Christensen et al., 2017). Vertical solid red line shows the timing of the single most abrupt shift in mean. Solid horizontal red lines show mean values before and after the changepoint. Vertical dashed red line shows the timing of the single most abrupt shift in slope and horizontal dashed red lines show trends before and after.

determinations (Figures 6d and 6e). Assuming the model is accurate, δ^2H_{C31} values display zero phase lag and significant (>0.60) spectral coherence with MS in the 41- and 100-kyr bands (Figure S4a in Supporting Information S1). BTB13 δ^2H_{C31} values are coherent and in-phase with the 23.5°N–23.5°S 21 June insolation gradient in the 41-kyr band (Figures 6d and 6e). δ^2H_{C31} values and the gradient are less strongly coherent in the 19-, 23-, and 100-kyr bands and phase relationships vary between 0 and 180°. δ^2H_{C31} values and the benthic $\delta^{18}O$ stack (Lisiecki & Raymo, 2005) are strongly coherent in the 41-kyr band in the upper 200 kyr (Marine Isotope Stages 103, G1, and G3) (Figure S4b in Supporting Information S1). δ^2H_{C31} values and 21 June insolation at 30°N are spectrally coherent in the 19–23, 41, and 100 kyr bands; they are weakly in-phase in the 41-kyr band but antiphased in the 19, 23, and 100 bands (Figure S4c in Supporting Information S1). 36–46 kyr bandpass filtered δ^2H_{C31} values are in-phase with the 41 kyr component of the 23.5°N–23.5°S 21 June insolation gradient (3.28–2.95 and 2.75–2.58 Ma) but out of phase with 36–46 kyr bandpass filtered benthic foraminiferal $\delta^{18}O$ values (Lisiecki & Raymo, 2005) and Arabian Sea (Herbert et al., 2015) and Southern Ocean (Martínez-Garcia et al., 2010) SSTs (Figure S5 in Supporting Information S1).

3.3. Indian Ocean Zonal Gradients During the Plio-Pleistocene

When limited to BTB13's timespan, western Australian NGR K % and XRF (K + Al)/Ca data exhibit clear drying changepoints around 3.03–3.08 Ma (Figure 7), in agreement with pollen-inferred western Australian drying about 3.0 (Martin & McMinn, 1994) to 2.9 Ma (Dodson & Macphail, 2004) as well as the wetter changepoint in BTB. While the BTB13 record only extends to ~2.6 Ma, the longer DSDP Site 231 and IODP Site U1478 δ^2H_{wax} records suggest drying in eastern African by 2.5 Ma (Liddy et al., 2016; Taylor et al., 2021).

Most Pliocene $\Delta SST_{W\text{-}E}$ data indicate an increase in the gradient between 3.05 and 2.95 Ma, followed by a gradual decrease until 2.6–2.5 Ma with a range in low-pass filtered $\Delta SST_{W\text{-}E}$ of ~5°C or ~1‰ (Figure S6 in Supporting Information S1). ODP Sites 709–763 Mg/Ca values are the exception—there are no major secular trends in $\Delta SST_{W\text{-}E}$, which only varies by ~1°C. As foraminiferal Mg/Ca might be affected by changing Plio-Pleistocene seawater Mg/Ca in addition to temperature (Evans et al., 2016; Fantle & DePaolo, 2006; Medina-Elizalde et al., 2008; O'Brien et al., 2014) and choice of depth versus carbonate saturation-based correction at the deeper Site 709C (Regenberg et al., 2006), we infer that Mg/Ca at Site 709C Mg/Ca measures SST less well than other proxies. In the later Pleistocene, $\Delta SST_{W\text{-}E}$ is stable from 2.2 to 1.2 Ma, declines until the latest Pleistocene, and increases sharply within the last 50–100 kyr (Figure S7 in Supporting Information S1).

Plio-Pleistocene IO $\Delta SST_{W\text{-}E}$ is not consistently driven by either the East or West IO. Warming/cooling changepoints are roughly simultaneous and of equal magnitude ($\Delta\delta^{18}O_p \approx 0.5‰$) around 3 Ma (Kaboth-Bahr & Mudelsee, 2022). Similarly, both western and eastern IO trends contribute to changes in late Pliocene TEX_{86} $\Delta SST_{W\text{-}E}$ (Figures S8a and S8b in Supporting Information S1). In the later Pleistocene, eastern IO warming is responsible for the collapse in $U^{k'}_{37}$ $\Delta SST_{W\text{-}E}$ around 0.8 Ma, but cooler glacial periods at Site 722 cause most $\Delta SST_{W\text{-}E}$ decline after 0.5 Ma (Figure S8d in Supporting Information S1).

On >100 kyr timescales, nine of 13 eastern African hydroclimate records (including BTB13 δ^2H_{C31} values) are significantly correlated ($p < 0.05$) with (non-Mg/Ca) $\Delta SST_{W\text{-}E}$. In eight of these nine, higher terrestrial moisture coincides with a larger $\Delta SST_{W\text{-}E}$; the exception is Lake Malawi Ca % (Johnson et al., 2016). Of the four Plio-Pleistocene records with paired δ^2H_{wax}-SST values, three are significantly ($p < 0.05$) and positively correlated such that warmer western IO SSTs are associated with higher precipitation. Of the four SST transects we compared to BTB13, precipitation and $\Delta SST_{W\text{-}E}$ are significantly and positively correlated in two

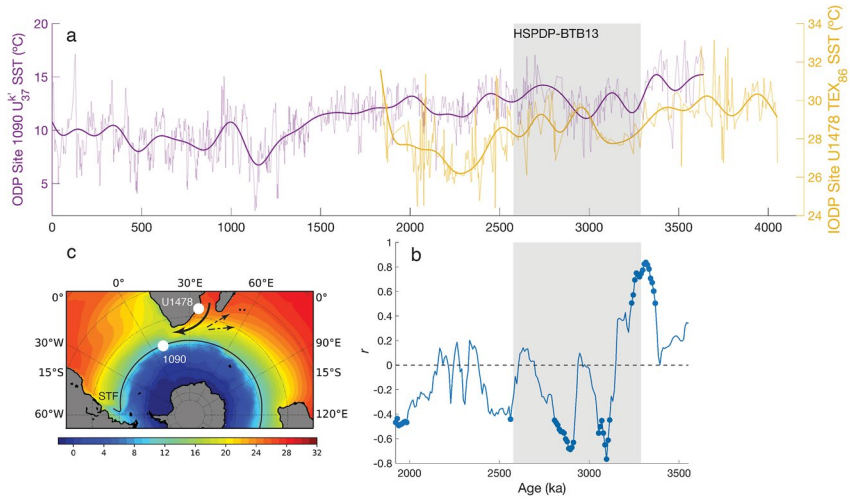

Figure 8. (a) Sea surface temperatures (SSTs) from ODP Site 1090 ($U^{k'}_{37}$) (Martínez-Garcia et al., 2010) (purple) and International Ocean Drilling Program Site U1478 (TEX_{86}) (Taylor et al., 2021) (gold). (b) A running 10-point Pearson's *r* of Site 1090 and U1478 SSTs. Filled circles indicate intervals where correlation is statistically significant ($p \leq 0.05$). Shading indicates the timespan of BTB13. (c) Locations of Sites 1090 and U1478, the modern-day subtropical front (Orsi et al., 1995), and the Agulhas leakage (thick arrow) and retroflection/return current (dashed arrows) (Bard & Rickaby, 2009; Graham & De Boer, 2013). Background is 0.25° × 0.25° gridded 1982–2010 average SSTs (Reynolds et al., 2007).

(Table 1). In short, BTB13 δ^2H_{C31} values and broader eastern African hydroclimate generally track IO $\Delta SST_{W\text{-}E}$ on extra-orbital (>100-kyr) timescales.

Since most individual IO SST records (Figure S8 in Supporting Information S1) and therefore $\Delta SST_{W\text{-}E}$ are too low-resolution to extract <100 kyr trends, we do not perform spectral analyses on either. The exception is ODP 722 (Herbert et al., 2015), which exhibits 19, 23, 41, and 100 kyr variance over the BTB13 timespan (Figure S9 in Supporting Information S1).

3.4. Coupling of Plio-Pleistocene Southern Ocean and Agulhas Temperatures

Site 1090 and U1478 SSTs are strongly positively correlated ($r = 0.2$ to 0.8) between 3.5 and 3.2 Ma but switch to anticorrelated ($r = -0.2$ to -0.5) from 3.1 Ma on. Correlations are statistically significant ($p < 0.05$) when *r* is >0.4 or <−0.4, particularly immediately prior to/after the changepoint at ∼3.1 Ma (Figure 8).

4. Discussion

4.1. Interpretation of BTB13 Paleoclimate Proxies and Data

While existing BTB13 data coherently demonstrate that the basin underwent significant hydrologic and environmental change, it is unclear if these events were localized or attributable to regional eastern African atmospheric circulation. Since leaf lipids are more broadly geographically sourced, they presumably record conditions beyond BTB; the high coherence between δ^2H_{C31} values and MS (Figure S4a in Supporting Information S1) suggests that local hydrology is largely controlled by regional climate and that δ^2H_{C31} values are primarily a function of the "amount effect," a range of atmospheric processes that result in the negative correlation observed between rainfall amount and its isotopic composition and the primary control on tropical eastern African δ^2H_{H2O} and thereby δ^2H_{wax} values (Dansgaard, 1964; Rozanski et al., 2013). Others include elevation, temperature, and moisture source.

While the timing of specific rifting events are poorly constrained (Macgregor, 2015), much of the major uplift had occurred by 13.5 Ma (Wichura et al., 2010). Terrestrial temperatures are largely unknown, but western IO SST records show 2–3°C sustained temperature change over BTB13's timespan (Figure S8 in Supporting Information S1), too small to explain the 60‰ range in δ^2H_{C31} values (Figures 2 and 4). Assuming little temperature or elevation change in the late Pliocene Baringo Basin, variations in moisture source (i.e., Congo vs. IO) are the only

other plausible driver of δ^2H_{H2O} change (Levin et al., 2009; Tierney et al., 2011), but the strong positive correlation and in-phase spectral coherence of δ^2H_{C31} values and MS (Figure S4a in Supporting Information S1) suggest that deuterium-depleted rainfall is indeed associated with higher erosion and runoff. The δ^2H_{C31} changepoint at 3 Ma also coincides with the first appearance of diatomites (Westover et al., 2021) and fish fossils (Billingsley et al., 2021) and thus deeper lakes in the region. These physical proxies should be insensitive to δ^2H_{H2O} change; this implies that enhanced precipitation drove fluctuations in lake levels, and therefore that δ^2H_{C31} values are a robust indicator of rainfall amount and actual changes in the local water budget.

4.2. Mechanisms Behind Indian Ocean Dipole-Like Behavior at 3 Ma

While IO $\Delta SST_{W\text{-}E}$ demonstrably influences eastern African hydrology on seasonal to glacial-interglacial timescales (Abram et al., 2008, 2020; Di Nezio et al., 2016; Konecky et al., 2014; Saji et al., 1999; Tierney et al., 2011, 2013; Ummenhofer et al., 2009; Webster et al., 1999), trans-IO Walker circulation has yet to be observed at the orbital scale. The coincidence of (opposing) African and Australian hydroclimate shifts and heightened $\Delta SST_{W\text{-}E}$ between 3.1 and 2.9 Ma suggests that the latter is driving the former. Here, we consider several possible mechanisms for increasing $\Delta SST_{W\text{-}E}$, including the restriction of the ITF current, iNHG-driven meridional migration of the ITCZ, and Antarctic-driven meridional migration of the STF.

The northwards drift of New Guinea-Australia and the growth of Halmahera in the Pliocene (Cane & Molnar, 2001) may have constricted Pacific-IO heat exchange via the ITF (Jochum et al., 2009; Rodgers et al., 2000; Sarnthein et al., 2018), replacing warm southern Pacific with cold northern Pacific water and increasing IO $\Delta SST_{W\text{-}E}$ (Kaboth-Bahr et al., 2021; Kaboth-Bahr & Mudelsee, 2022). However, proxy data indicate no significant change in Pacific $\Delta SST_{W\text{-}E}$ until ~1.7 Ma (Wara et al., 2005), and eastern IO cooling associated with ITF restriction is thought to have occurred by 3.5 Ma (Auer et al., 2019; Gourlan et al., 2008; Karas et al., 2011), well before the BTB13/Site U1463 ~3 Ma changepoint. Furthermore, if the ~3 Ma changepoints in eastern Africa and western Australia were the result of permanent ITF restriction, IO Walker Circulation should have been permanently affected, but several measures of SST and hydroclimate rebound within ~500 kyr (Figure S8 in Supporting Information S1). Finally, late Pliocene $U^{k'}_{37}$ SSTs at ODP Site 722 exhibit no trend (Herbert et al., 2015), suggesting that changes in the Leeuwin Current do not necessarily propagate across the entire IO (van der Lubbe et al., 2021).

Similarly, high-northern latitude cooling can influence tropical rainfall through several processes, including latitudinal migration of the ITCZ (Broccoli et al., 2006; Chiang & Bitz, 2005; Chiang et al., 2003; Lechleitner et al., 2017; Mischell & Lee, 2022). With few exceptions (Sarnthein et al., 2009), North Atlantic SSTs exhibit little secular change in the late Pliocene (Clotten et al., 2018; Lawrence et al., 2009; Naafs et al., 2020). No global (Lisiecki & Raymo, 2005) or North Atlantic (Bartoli et al., 2005; Kleiven et al., 2002) benthic ^{18}O-enrichment or IRD pulses (Bailey et al., 2013) occur until 2.9–2.7 Ma. Therefore, the changepoints in the Baringo Basin and Site U1463 postdate the tectonic reorganization of Indonesia but predate iNHG.

We propose that Antarctic cooling and the northward migration of the STF drove simultaneous temperature change on both ends of the IO, thereby enhancing the eastern Africa-western Australia precipitation dipole at ~3 Ma. The Agulhas current, which transfers warm surface waters from the IO to the Atlantic around the Cape of Good Hope, weakens during glacial periods, as the STF approaches South Africa and weakens Agulhas leakage (Bard & Rickaby, 2009; Caley et al., 2012). Surface warmth retroflects along the Agulhas Return Current and heats the western IO (Civel-Mazens et al., 2021). Thus, Southern Hemisphere glaciation/STF migration steepens IO $\Delta SST_{W\text{-}E}$, causing a wetter coastal equatorial eastern Africa during cool intervals such as the LGM (Di Nezio et al., 2016).

Thus far, this teleconnection has only been demonstrated in the mid-late Pleistocene. The initiation of anticor-related ODP Site 1090 and IODP Site U1478 SSTs about 3.1 Ma (Figure 8) corresponds to other late Pliocene Southern Ocean cooling steps including the emergence of persistent Antarctic summer sea ice around 3.03 Ma (Riesselman & Dunbar, 2013), cooler $U^{k'}_{37}$ SSTs at Tasman Sea DSDP Site 593 (McClymont et al., 2016) and ODP Site 1125 (Fedorov et al., 2015), and increased STF-diagnostic nannofossils at Tasman Sea ODP Site 1172 (Ballegeer et al., 2012) around 3.1 Ma, interpreted as evidence for the northwards migration of the STF (McClymont et al., 2016). Prior to ~3.3 Ma, the STF perhaps did not approach near enough to the Cape of Good Hope to significantly affect the Agulhas, and 1090 and U1478 temperatures covaried. The causes of these STF movements are possibly related to Northern Component Water leakage at ~3 Ma (Poore et al., 2006) but require additional study.

4.3. Plio-Pleistocene Orbital Variability in the Baringo Basin

Although the dominant orbital periodicities in the more numerous Pleistocene-Holocene eastern African hydroclimate records are 19–23 kyr precession, the obliquity and eccentricity components of extant Plio-Pleistocene data suggest a more complex set of forcings, or at least changing dynamics over time (Section 1.2). The strong obliquity signal in BTB13 δ^2H_{C31} values (Figure 6)—the highest-resolution Plio-Pleistocene leaf wax isotope record to date—further signifies hydroclimatic influences outside of local insolation. Given that age model uncertainties are larger than the periodicity of precession over much of the core, we cannot conclusively prove that precession is absent or present, so we focus on the longer (40–100 kyr) cycles, which should be relatively unaffected given the highly linear long-term sedimentation rates (Figure 2a); for precession to be present but obscured throughout would require highly *non*linear sedimentation between obliquity minima/maxima.

Assuming that the BTB13 age model is accurate on $>10^1$ kyr timescales, we propose that 41 kyr variability in Plio-Pleistocene eastern African rainfall is set by the interhemispheric 21 June 23.5°N–23.5°S insolation gradient. The gradient is a better candidate for the source of obliquity variance in BTB13 δ^2H_{C31} values than variations in global ice volume and temperature, Arabian Sea SSTs, or Southern Ocean SSTs (Figure S5 in Supporting Information S1), since the 41 kyr component of δ^2H_{C31} values is out of phase with marine 41 kyr variance (Figures S4 and S5 in Supporting Information S1) but coherent with 0° phase lag with the insolation gradient (Figure 6). This relationship could explain why 41-kyr cycles are strongly present in BTB13 and Site U1478 δ^2H_{wax} values and Site U1463 K %, before iNHG, and in North African precipitation after the mid-Pleistocene transition (O'Mara et al., 2022), even when obliquity is not the dominant frequency of the benthic $\delta^{18}O$ record (Lisiecki & Raymo, 2007).

The strongly 100-kyr component of the δ^2H_{C31} record in the 2.75–2.95 interval has several potential sources. Eccentricity typically modulates the strength of precession (Foerster et al., 2022; Trauth et al., 2007), but BTB13's δ^2H_{C31} spectrum lacks 21-kyr periodicity, as do the MS and Si/Ti spectra until 2.68 Ma (Figure S3 in Supporting Information S1). (Age model uncertainties in BTB13 range up to ±50 kyr in the middle 300 kyr [3–2.7 Ma] (Deino et al., 2021), greater than 1–2 precession cycles.) 100 kyr periodicity, which is also observed in southern Ethiopian hydroclimate post-MPT (Foerster et al., 2022), could also be the result of 100-kyr ENSO-like fluctuations in pan-African moisture balance (Kaboth-Bahr et al., 2021), perhaps transmitted via the IO, which also displays some 100 kyr variance in the late Pliocene (Figure S9 in Supporting Information S1), although it is unclear whether teleconnections between tropical Pacific SST gradients and African moisture balance exist prior to the establishment of global ∼100-kyr variability around 800 ka (Lisiecki & Raymo, 2005) or zonal gradients in equatorial Pacific SSTs at 1.7 Ma (Wara et al., 2005). It is also noteworthy that eccentricity only appears to dominate when cross-equatorial insolation gradient variability is at its most muted, suggesting a more complex interplay of orbital forcings than previously realized.

The spectral imprint of IO SSTs and $\Delta SST_{W\text{-}E}$ on eastern African precipitation is also difficult to quantify on orbital (<100–200 kyr) timescales because most Plio-Pleistocene IO records are not sufficiently resolved to extract 19-, 23-, or even 41-kyr cyclicity, compounded by the interpolation required to calculate $\Delta SST_{W\text{-}E}$. δ^2H_{C31} values remain most coherent with the cross-equatorial insolation difference, suggesting that they represent the hybrid influences of the meridional insolation gradient on orbital and IO Walker Circulation on supra-orbital (and possibly orbital) timescales. Ultimately, higher-resolution paired terrestrial-marine archives are likely required to fully disentangle these processes and assess if eastern African hydroclimate derives its 19–100-kyr components from the IO.

5. Conclusions

Geochemical (Si/Ti, δ^2H_{C31} values) and physical (MS) proxy data from BTB13 show an increase in moisture around 3 Ma as well as prominent 41-kyr periodicity between ∼3.3 and 2.6 Ma. Many eastern African hydroclimate records contain a dominant 21-kyr periodicity associated with orbital precession (Caley et al., 2018; Foerster et al., 2022; Joordens et al., 2011; Lupien et al., 2018, 2021, 2022; Nutz et al., 2017; Partridge et al., 1997; Yost et al., 2021). Proxy evidence, and particularly sedimentologic records of lake levels, from BTB13 do demonstrate a strong influence of precession in the Baringo Basin; our δ^2H_{C31} record likely cannot resolve this periodicity. Nevertheless, the 41-kyr precipitation cycle in BTB appears coupled to the cross-equatorial insolation gradient, suggesting that additional controls beyond hemispheric seasonal insolation forcing are important to equatorial eastern African rainfall.

BTB13 δ^2H_{C31} values are positively correlated with zonal $\delta^{18}O_p$ and SST gradients across the southern and central IO and, combined with drying in western Australia between 3.1 and 3 Ma (postdating the closure of the Indonesian Seaway), suggest that a Walker Circulation-driven precipitation dipole has governed trans-IO climate since at least the late Pliocene—over a million years before the Pacific (Wara et al., 2005). This implies that a high $\Delta SST_{W\text{-}E}$ overrode the thermodynamic effects of global cooling and drying in eastern Africa across the Plio-Pleistocene boundary. In contrast, mid- to late Pleistocene cooling (1.1 Ma-present) and a $\Delta SST_{W\text{-}E}$ decline generally resulted in a drier eastern Africa (Caley et al., 2018; Foerster et al., 2022; Owen et al., 2018). The $\Delta SST_{W\text{-}E}$ increase around 3 Ma (+3 to 5°C) is comparable to present-day $\Delta SST_{W\text{-}E}$ values associated with major IOZD events (Abram et al., 2008), while the ∼−11.5‰ δ^2H_{precip} shift at ∼3 Ma is roughly equivalent to ¼ of modern annual variance (Figure 3). If anthropogenic warming enhances $\Delta SST_{W\text{-}E}$ and thereby precipitation similarly to ∼3 Ma, adaptation and mitigation efforts must account for the higher likelihood of extreme wet events and increased mean annual rainfall in equatorial eastern Africa (Ogega et al., 2020; Shongwe et al., 2011).

Data Availability Statement

BTB13 δ^2H_{wax}, $\delta^{13}C_{wax}$, MS, and XRF Si/Ti data presented here are available from the National Oceanic and Atmospheric Administration's Paleoclimatology Data service (Mitsunaga et al., 2023).

Acknowledgments
The authors wish to thank Wylie De Groff and Adin Richards for additional sample processing; Ewerton Santos for his efforts in maintaining the GC-IRMS and method optimization; the LacCore and HSPDP communities; Stefanie Kaboth-Bahr for several key conversations aboard the *JOIDES Resolution*; Xiaojing Du for climate model assistance; and the other members of the Russell and Herbert labs at Brown. This work was supported by National Science Foundation Grants 1338553, 1322017, and 1826938. Bryce Mitsunaga was funded by an NSF Graduate Research Fellowship (Grant DGE-1144087). This is publication #54 of the Hominin Sites and Paleolakes Drilling Project.

References

Abram, N. J., Gagan, M. K., Cole, J. E., Hantoro, W. S., & Mudelsee, M. (2008). Recent intensification of tropical climate variability in the Indian Ocean. *Nature Geoscience*, *1*(12), 849–853. https://doi.org/10.1038/ngeo357

Abram, N. J., Wright, N. M., Ellis, B., Dixon, B. C., Wurtzel, J. B., England, M. H., et al. (2020). Coupling of Indo-Pacific climate variability over the last millennium. *Nature*, *579*(7799), 385–392. https://doi.org/10.1038/s41586-020-2084-4

An, S.-I., Park, H.-J., Kim, S.-K., Shin, J., Yeh, S.-W., & Kug, J.-S. (2022). Intensity changes of Indian Ocean dipole mode in a carbon dioxide removal scenario. *Npj Climate and Atmospheric Science*, *5*(1), 1–8. https://doi.org/10.1038/s41612-022-00246-6

Auer, G., De Vleeschouwer, D., & Christensen, B. A. (2020). Toward a robust Plio-Pleistocene chronostratigraphy for ODP Site 762. *Geophysical Research Letters*, *47*(3), e2019GL085198. https://doi.org/10.1029/2019GL085198

Auer, G., De Vleeschouwer, D., Smith, R. A., Bogus, K., Groeneveld, J., Grunert, P., et al. (2019). Timing and pacing of Indonesian Throughflow restriction and its connection to Late Pliocene climate shifts. *Paleoceanography and Paleoclimatology*, *34*(4), 635–657. https://doi.org/10.1029/2018PA003512

Bailey, I., Hole, G. M., Foster, G. L., Wilson, P. A., Storey, C. D., Trueman, C. N., & Raymo, M. E. (2013). An alternative suggestion for the Pliocene onset of major northern hemisphere glaciation based on the geochemical provenance of North Atlantic Ocean ice-rafted debris. *Quaternary Science Reviews*, *75*, 181–194. https://doi.org/10.1016/j.quascirev.2013.06.004

Ballegeer, A.-M., Flores, J. A., Sierro, F. J., & Andersen, N. (2012). Monitoring fluctuations of the subtropical front in the Tasman Sea between 3.45 and 2.45Ma (ODP site 1172). *Palaeogeography, Palaeoclimatology, Palaeoecology*, *313–314*, 215–224. https://doi.org/10.1016/j.palaeo.2011.11.001

Bard, E., & Rickaby, R. E. M. (2009). Migration of the subtropical front as a modulator of glacial climate. *Nature*, *460*(7253), 380–383. https://doi.org/10.1038/nature08189

Bartoli, G., Sarnthein, M., Weinelt, M., Erlenkeuser, H., Garbe-Schönberg, D., & Lea, D. W. (2005). Final closure of Panama and the onset of northern hemisphere glaciation. *Earth and Planetary Science Letters*, *237*(1–2), 33–44. https://doi.org/10.1016/j.epsl.2005.06.020

Bessems, I., Verschuren, D., Russell, J. M., Hus, J., Mees, F., & Cumming, B. F. (2008). Palaeolimnological evidence for widespread late 18th century drought across equatorial East Africa. *Palaeogeography, Palaeoclimatology, Palaeoecology*, *259*(2), 107–120. https://doi.org/10.1016/j.palaeo.2007.10.002

Billingsley, A. L., Reinthal, P., Dettman, D. L., Kingston, J. D., Deino, A. L., Ortiz, K., et al. (2021). $\delta^{13}C$ records from fish fossils as paleo-indicators of ecosystem responses to lake levels in the Plio-Pleistocene lakes of Tugen Hills, Kenya. *Palaeogeography, Palaeoclimatology, Palaeoecology*, *570*, 109466. https://doi.org/10.1016/j.palaeo.2019.109466

Bloemendal, J., & deMenocal, P. (1989). Evidence for a change in the periodicity of tropical climate cycles at 2.4 Myr from whole-core magnetic susceptibility measurements. *Nature*, *342*(6252), 897–900. https://doi.org/10.1038/342897a0

Bonnefille, R. (1983). Evidence for a cooler and drier climate in the Ethiopian uplands towards 2.5 Myr ago. *Nature*, *303*(5917), 487–491. https://doi.org/10.1038/303487a0

Bosmans, J. H. C., Hilgen, F. J., Tuenter, E., & Lourens, L. J. (2015). Obliquity forcing of low-latitude climate. *Climate of the Past*, *11*(10), 1335–1346. https://doi.org/10.5194/cp-11-1335-2015

Bray, E. E., & Evans, E. D. (1961). Distribution of n-paraffins as a clue to recognition of source beds. *Geochimica et Cosmochimica Acta*, *22*(1), 2–15. https://doi.org/10.1016/0016-7037(61)90069-2

Broccoli, A. J., Dahl, K. A., & Stouffer, R. J. (2006). Response of the ITCZ to Northern Hemisphere cooling. *Geophysical Research Letters*, *33*(1), L01702. https://doi.org/10.1029/2005GL024546

Brown, E. T. (2015). Estimation of biogenic silica concentrations using scanning XRF: Insights from studies of Lake Malawi sediments. In I. W. Croudace & R. G. Rothwell (Eds.), *Micro-XRF studies of sediment cores: Applications of a non-destructive tool for the environmental sciences* (pp. 267–277). Springer Netherlands. https://doi.org/10.1007/978-94-017-9849-5_9

Bush, R. T., & McInerney, F. A. (2013). Leaf wax *n*-alkane distributions in and across modern plants: Implications for paleoecology and chemotaxonomy. *Geochimica et Cosmochimica Acta*, *117*, 161–179. https://doi.org/10.1016/j.gca.2013.04.016

Cai, W., Santoso, A., Wang, G., Weller, E., Wu, L., Ashok, K., et al. (2014). Increased frequency of extreme Indian Ocean Dipole events due to greenhouse warming. *Nature*, *510*(7504), 254–258. https://doi.org/10.1038/nature13327

Cai, W., Sullivan, A., & Cowan, T. (2009). Climate change contributes to more frequent consecutive positive Indian Ocean Dipole events. *Geophysical Research Letters*, *36*(23), L23704. https://doi.org/10.1029/2009GL040163

Cai, W., Zheng, X.-T., Weller, E., Collins, M., Cowan, T., Lengaigne, M., et al. (2013). Projected response of the Indian Ocean Dipole to greenhouse warming. *Nature Geoscience*, *6*(12), 999–1007. https://doi.org/10.1038/ngeo2009

Caley, T., Extier, T., Collins, J. A., Schefuß, E., Dupont, L., Malaizé, B., et al. (2018). A two-million-year-long hydroclimatic context for hominin evolution in southeastern Africa. *Nature*, *560*(7716), 76–79. https://doi.org/10.1038/s41586-018-0309-6

Caley, T., Giraudeau, J., Malaizé, B., Rossignol, L., & Pierre, C. (2012). Agulhas leakage as a key process in the modes of Quaternary climate changes. *Proceedings of the National Academy of Sciences*, *109*(18), 6835–6839. https://doi.org/10.1073/pnas.1115545109

Campisano, C., Cohen, A., Arrowsmith, R., Asrat, A., Behrensmeyer, A., Brown, E., et al. (2017). The Hominin Sites and Paleolakes Drilling Project: High-resolution paleoclimate records from the east African rift system and their implications for understanding the environmental context of hominin evolution. *PaleoAnthropology*, *2017*, 1–43. https://doi.org/10.4207/PA.2017.ART104

Cane, M. A., & Molnar, P. (2001). Closing of the Indonesian seaway as a precursor to east African aridification around 3–4 million years ago. *Nature*, *411*(6834), 157–162. https://doi.org/10.1038/35075500

Castañeda, I. S., Caley, T., Dupont, L., Kim, J.-H., Malaizé, B., & Schouten, S. (2016). Middle to Late Pleistocene vegetation and climate change in subtropical southern East Africa. *Earth and Planetary Science Letters*, *450*, 306–316. https://doi.org/10.1016/j.epsl.2016.06.049

Cerling, T. E. (1992). Development of grasslands and savannas in east Africa during the Neogene. *Palaeogeography, Palaeoclimatology, Palaeoecology*, *97*(3), 241–247. https://doi.org/10.1016/0031-0182(92)90211-M

Chapman, G. R., & Brook, M. (1978). Chronostratigraphy of the Baringo Basin, Kenya. *Geological Society, London, Special Publications*, *6*(1), 207–223. https://doi.org/10.1144/GSL.SP.1978.006.01.16

Chen, J., Farrell, J. W., Murray, D. W., & Prell, W. L. (1995). Timescale and paleoceanographic implications of a 3.6 m.y. Oxygen isotope record from the northeast Indian Ocean (Ocean Drilling Program Site 758). *Paleoceanography*, *10*(1), 21–47. https://doi.org/10.1029/94PA02290

Chiang, J. C. H., Biasutti, M., & Battisti, D. S. (2003). Sensitivity of the Atlantic Intertropical Convergence Zone to last glacial maximum boundary conditions. *Paleoceanography*, *18*(4), 1094. https://doi.org/10.1029/2003PA000916

Chiang, J. C. H., & Bitz, C. M. (2005). Influence of high latitude ice cover on the marine Intertropical Convergence Zone. *Climate Dynamics*, *25*(5), 477–496. https://doi.org/10.1007/s00382-005-0040-5

Christensen, B. A., Renema, W., Henderiks, J., De Vleeschouwer, D., Groeneveld, J., Castañeda, I. S., et al. (2017). Indonesian Throughflow drove Australian climate from humid Pliocene to arid Pleistocene. *Geophysical Research Letters*, *44*(13), 6914–6925. https://doi.org/10.1002/2017GL072977

Civel-Mazens, M., Crosta, X., Cortese, G., Michel, E., Mazaud, A., Ther, O., et al. (2021). Impact of the Agulhas Return Current on the oceanography of the Kerguelen Plateau region, Southern Ocean, over the last 40 Kyrs. *Quaternary Science Reviews*, *251*, 106711. https://doi.org/10.1016/j.quascirev.2020.106711

Clotten, C., Stein, R., Fahl, K., & De Schepper, S. (2018). Seasonal sea ice cover during the warm Pliocene: Evidence from the Iceland Sea (ODP Site 907). *Earth and Planetary Science Letters*, *481*, 61–72. https://doi.org/10.1016/j.epsl.2017.10.011

Cohen, A. S., Campisano, C., Arrowsmith, R., Asrat, A., Behrensmeyer, A. K., Deino, A., et al. (2016). The Hominin Sites and Paleolakes Drilling Project: Inferring the environmental context of human evolution from eastern African rift lake deposits. *Scientific Drilling*, *21*, 1–16. https://doi.org/10.5194/sd-21-1-2016

Cohen, A. S., Stone, J. R., Beuning, K. R. M., Park, L. E., Reinthal, P. N., Dettman, D., et al. (2007). Ecological consequences of early Late Pleistocene megadroughts in tropical Africa. *Proceedings of the National Academy of Sciences*, *104*(42), 16422–16427. https://doi.org/10.1073/pnas.0703873104

Collins, J. A., Schefuß, E., Mulitza, S., Prange, M., Werner, M., Tharammal, T., et al. (2013). Estimating the hydrogen isotopic composition of past precipitation using leaf-waxes from western Africa. *Quaternary Science Reviews*, *65*, 88–101. https://doi.org/10.1016/j.quascirev.2013.01.007

Crocker, A. J., Naafs, B. D. A., Westerhold, T., James, R. H., Cooper, M. J., Röhl, U., et al. (2022). Astronomically controlled aridity in the Sahara since at least 11 million years ago. *Nature Geoscience*, *15*(8), 671–676. https://doi.org/10.1038/s41561-022-00990-7

Dansgaard, W. (1964). Stable isotopes in precipitation. *Tellus*, *16*(4), 436–468. https://doi.org/10.1111/j.2153-3490.1964.tb00181.x

Deino, A. L., & Hill, A. (2002). $^{40}Ar/^{39}Ar$ dating of Chemeron Formation strata encompassing the site of hominid KNM-BC 1, Tugen Hills, Kenya. *Journal of Human Evolution*, *42*(1–2), 141–151. https://doi.org/10.1006/jhev.2001.0522

Deino, A. L., Kingston, J., Glen, J., Edgar, R., & Hill, A. (2006). Precessional forcing of lacustrine sedimentation in the late Cenozoic Chemeron Basin, Central Kenya Rift, and calibration of the Gauss/Matuyama boundary. *Earth and Planetary Science Letters*, *247*(1–2), 41–60. https://doi.org/10.1016/j.epsl.2006.04.009

Deino, A. L., Sier, M. J., Garello, D. I., Keller, C. B., Kingston, J. D., Scott, J. J., et al. (2021). Chronostratigraphy of the Baringo-Tugen Hills-Barsemoi (HSPDP-BTB13-1A) core – 40Ar/39Ar dating, magnetostratigraphy, tephrostratigraphy, sequence stratigraphy and Bayesian age modeling. *Palaeogeography, Palaeoclimatology, Palaeoecology*, *570*, 109519. https://doi.org/10.1016/j.palaeo.2019.109519

deMenocal, P. B. (1995). Plio-Pleistocene African climate. *Science*, *270*(5233), 53–59. https://doi.org/10.1126/science.270.5233.53

deMenocal, P. B. (2004). African climate change and faunal evolution during the Pliocene–Pleistocene. *Earth and Planetary Science Letters*, *220*(1–2), 3–24. https://doi.org/10.1016/S0012-821X(04)00003-2

de Oliveira, C. P., Aímola, L., Ambrizzi, T., & Freitas, A. C. V. (2018). The influence of the regional Hadley and Walker circulations on precipitation patterns over Africa in El Niño, La Niña, and neutral years. *Pure and Applied Geophysics*, *175*(6), 2293–2306. https://doi.org/10.1007/s00024-018-1782-4

De Vleeschouwer, D., Peral, M., Marchegiano, M., Füllberg, A., Meinicke, N., Pälike, H., et al. (2022). Plio-Pleistocene Perth Basin water temperatures and Leeuwin Current dynamics (Indian Ocean) derived from oxygen and clumped-isotope paleothermometry. *Climate of the Past*, *18*(5), 1231–1253. https://doi.org/10.5194/cp-18-1231-2022

Dillon, J. T., & Huang, Y. (2015). TEXPRESS v1.0: A MATLAB toolbox for efficient processing of GDGT LC–MS data. *Organic Geochemistry*, *79*, 44–48. https://doi.org/10.1016/j.orggeochem.2014.11.009

Di Nezio, P. N., Timmermann, A., Tierney, J. E., Jin, F.-F., Otto-Bliesner, B., Rosenbloom, N., et al. (2016). The climate response of the Indo-Pacific warm pool to glacial sea level. *Paleoceanography*, *31*(6), 866–894. https://doi.org/10.1002/2015PA002890

Dodson, J. R., & Macphail, M. K. (2004). Palynological evidence for aridity events and vegetation change during the Middle Pliocene, a warm period in Southwestern Australia. *Global and Planetary Change*, *41*(3), 285–307. https://doi.org/10.1016/j.gloplacha.2004.01.013

Eglinton, G., & Hamilton, R. J. (1967). Leaf epicuticular waxes. *Science*, *156*(3780), 1322–1335. https://doi.org/10.1126/science.156.3780.1322

Eglinton, T. I., & Eglinton, G. (2008). Molecular proxies for paleoclimatology. *Earth and Planetary Science Letters*, *275*(1), 1–16. https://doi.org/10.1016/j.epsl.2008.07.012

Emeis, K.-C., Sakamoto, T., Wehausen, R., & Brumsack, H.-J. (2000). The sapropel record of the eastern Mediterranean Sea—Results of Ocean Drilling Program Leg 160. *Palaeogeography, Palaeoclimatology, Palaeoecology*, *158*(3), 371–395. https://doi.org/10.1016/S0031-0182(00)00059-6

Evans, D., Brierley, C., Raymo, M. E., Erez, J., & Müller, W. (2016). Planktic foraminifera shell chemistry response to seawater chemistry: Pliocene–Pleistocene seawater Mg/Ca, temperature and sea level change. *Earth and Planetary Science Letters*, *438*, 139–148. https://doi.org/10.1016/j.epsl.2016.01.013

Fantle, M. S., & DePaolo, D. J. (2006). Sr isotopes and pore fluid chemistry in carbonate sediment of the Ontong Java Plateau: Calcite recrystallization rates and evidence for a rapid rise in seawater Mg over the last 10 million years. *Geochimica et Cosmochimica Acta*, *70*(15), 3883–3904. https://doi.org/10.1016/j.gca.2006.06.009

Farrell, J., & Janecek, T. (1991). Late Neogene Paleoceanography and Paleoclimatology of the Northeast Indian Ocean (Site 758). *Proceedings of the Ocean Drilling Program, Scientific Results*, *121*, 297–355. https://doi.org/10.2973/ODP.PROC.SR.121.124.1991

Feakins, S. J., deMenocal, P. B., & Eglinton, T. I. (2005). Biomarker records of late Neogene changes in northeast African vegetation. *Geology*, *33*(12), 977–980. https://doi.org/10.1130/G21814.1

Fedorov, A. V., Burls, N. J., Lawrence, K. T., & Peterson, L. C. (2015). Tightly linked zonal and meridional sea surface temperature gradients over the past five million years. *Nature Geoscience*, *8*(12), 975–980. https://doi.org/10.1038/ngeo2577

Foerster, V., Asrat, A., Bronk Ramsey, C., Brown, E. T., Chapot, M. S., Deino, A., et al. (2022). Pleistocene climate variability in eastern Africa influenced hominin evolution. *Nature Geoscience*, *15*(10), 1–7. https://doi.org/10.1038/s41561-022-01032-y

Garelick, S., Russell, J. M., Dee, S., Verschuren, D., & Olago, D. O. (2021). Atmospheric controls on precipitation isotopes and hydroclimate in high-elevation regions in Eastern Africa since the Last Glacial Maximum. *Earth and Planetary Science Letters*, *567*, 116984. https://doi.org/10.1016/j.epsl.2021.116984

Garello, D. I. (2019). Tephrostratigraphy of Pliocene drill cores from Kenya and Ethiopia, and Pleistocene exposures in the Ledi-Geraru research project area. In *Ethiopia: Geological context for the evolution of Australopithecus and Homo*. Arizona State University. Retrieved from https://keep.lib.asu.edu/items/157478

Gasse, F. (2000). Hydrological changes in the African tropics since the Last Glacial Maximum. *Quaternary Science Reviews*, *19*(1), 189–211. https://doi.org/10.1016/S0277-3791(99)00061-X

Goddard, L., & Graham, N. E. (1999). Importance of the Indian Ocean for simulating rainfall anomalies over eastern and southern Africa. *Journal of Geophysical Research*, *104*(D16), 19099–19116. https://doi.org/10.1029/1999JD900326

Gourlan, A. T., Meynadier, L., & Allègre, C. J. (2008). Tectonically driven changes in the Indian Ocean circulation over the last 25 Ma: Neodymium isotope evidence. *Earth and Planetary Science Letters*, *267*(1), 353–364. https://doi.org/10.1016/j.epsl.2007.11.054

Graham, R. M., & De Boer, A. M. (2013). The dynamical subtropical front. *Journal of Geophysical Research: Oceans*, *118*(10), 5676–5685. https://doi.org/10.1002/jgrc.20408

Griffin, D. L. (1999). The late Miocene climate of northeastern Africa: Unravelling the signals in the sedimentary succession. *Journal of the Geological Society*, *156*(4), 817–826. https://doi.org/10.1144/gsjgs.156.4.0817

He, Y., Wang, H., & Liu, Z. (2021). Development of the Leeuwin Current on the northwest shelf of Australia through the Pliocene-Pleistocene period. *Earth and Planetary Science Letters*, *559*, 116767. https://doi.org/10.1016/j.epsl.2021.116767

Herbert, T. D., Ng, G., & Cleaveland Peterson, L. (2015). Evolution of Mediterranean sea surface temperatures 3.5–1.5 Ma: Regional and hemispheric influences. *Earth and Planetary Science Letters*, *409*, 307–318. https://doi.org/10.1016/j.epsl.2014.10.006

Herbert, T. D., Peterson, L. C., Lawrence, K. T., & Liu, Z. (2010). Tropical ocean temperatures over the past 3.5 million years. *Science*, *328*(5985), 1530–1534. https://doi.org/10.1126/science.1185435

Herrmann, S. M., & Mohr, K. I. (2011). A continental-scale classification of rainfall seasonality regimes in Africa based on gridded precipitation and land surface temperature products. *Journal of Applied Meteorology and Climatology*, *50*(12), 2504–2513. https://doi.org/10.1175/JAMC-D-11-024.1

Hilgen, F. (1991). Astronomical calibration of Gauss to Matuyama sapropels in the Mediterranean and implication for the Geomagnetic Polarity Time Scale. *Earth and Planetary Science Letters*, *104*(2), 226–244. https://doi.org/10.1016/0012-821X(91)90206-W

Hill, A., Curtis, G., & Drake, R. (1986). Sedimentary stratigraphy of the Tugen Hills, Baringo, Kenya. *Geological Society, London, Special Publications*, *25*(1), 285–295. https://doi.org/10.1144/GSL.SP.1986.025.01.23

Hounslow, M. W., & Maher, B. A. (1999). Source of the climate signal recorded by magnetic susceptibility variations in Indian Ocean sediments. *Journal of Geophysical Research*, *104*(B3), 5047–5061. https://doi.org/10.1029/1998JB900085

IAEA/WMO. (2023). *Global network of isotopes in precipitation*. The GNIP Database. Retrieved from https://nucleus.iaea.org/wiser

Jochum, M., Fox-Kemper, B., Molnar, P. H., & Shields, C. (2009). Differences in the Indonesian seaway in a coupled climate model and their relevance to Pliocene climate and El Niño. *Paleoceanography*, *24*(1), PA1212. https://doi.org/10.1029/2008PA001678

Johnson, T. C., Brown, E. T., & Shi, J. (2011). Biogenic silica deposition in Lake Malawi, East Africa over the past 150,000 years. *Palaeogeography, Palaeoclimatology, Palaeoecology*, *303*(1), 103–109. https://doi.org/10.1016/j.palaeo.2010.01.024

Johnson, T. C., Werne, J. P., Brown, E. T., Abbott, A., Berke, M., Steinman, B. A., et al. (2016). A progressively wetter climate in southern East Africa over the past 1.3 million years. *Nature*, *537*(7619), 220–224. https://doi.org/10.1038/nature19065

Joordens, J. C. A., Vonhof, H. B., Feibel, C. S., Lourens, L. J., Dupont-Nivet, G., van der Lubbe, J. H. J. L., et al. (2011). An astronomically-tuned climate framework for hominins in the Turkana Basin. *Earth and Planetary Science Letters*, *307*(1), 1–8. https://doi.org/10.1016/j.epsl.2011.05.005

Kaboth-Bahr, S., Gosling, W. D., Vogelsang, R., Bahr, A., Scerri, E. M. L., Asrat, A., et al. (2021). Paleo-ENSO influence on African environments and early modern humans. *Proceedings of the National Academy of Sciences*, *118*(23), e2018277118. https://doi.org/10.1073/pnas.2018277118

Kaboth-Bahr, S., & Mudelsee, M. (2022). The multifaceted history of the Walker Circulation during the Plio-Pleistocene. *Quaternary Science Reviews*, *286*, 107529. https://doi.org/10.1016/j.quascirev.2022.107529

Karas, C., Nürnberg, D., Gupta, A. K., Tiedemann, R., Mohan, K., & Bickert, T. (2009). Mid-Pliocene climate change amplified by a switch in Indonesian Subsurface Throughflow. *Nature Geoscience*, *2*(6), 434–438. https://doi.org/10.1038/ngeo520

Karas, C., Nürnberg, D., Tiedemann, R., & Garbe-Schönberg, D. (2011). Pliocene Indonesian Throughflow and Leeuwin Current dynamics: Implications for Indian Ocean polar heat flux. *Paleoceanography*, *26*(2), PA2217. https://doi.org/10.1029/2010PA001949

Killick, R., Fearnhead, P., & Eckley, I. A. (2012). Optimal detection of changepoints with a linear computational cost. *Journal of the American Statistical Association*, *107*(500), 1590–1598. https://doi.org/10.1080/01621459.2012.737745

Kingston, J. D., Deino, A. L., Edgar, R. K., & Hill, A. (2007). Astronomically forced climate change in the Kenyan Rift Valley 2.7–2.55 Ma: Implications for the evolution of early hominin ecosystems. *Journal of Human Evolution*, *53*(5), 487–503. https://doi.org/10.1016/j.jhevol.2006.12.007

Kleiven, H. F., Jansen, E., Fronval, T., & Smith, T. M. (2002). Intensification of Northern Hemisphere glaciations in the circum Atlantic region (3.5–2.4 Ma) – Ice-rafted detritus evidence. *Palaeogeography, Palaeoclimatology, Palaeoecology*, *184*(3), 213–223. https://doi.org/10.1016/S0031-0182(01)00407-2

Konecky, B., Russell, J., & Bijaksana, S. (2016). Glacial aridity in central Indonesia coeval with intensified monsoon circulation. *Earth and Planetary Science Letters*, *437*, 15–24. https://doi.org/10.1016/j.epsl.2015.12.037

Konecky, B., Russell, J., Vuille, M., & Rehfeld, K. (2014). The Indian Ocean Zonal Mode over the past millennium in observed and modeled precipitation isotopes. *Quaternary Science Reviews*, *103*, 1–18. https://doi.org/10.1016/j.quascirev.2014.08.019

Kuechler, R., Dupont, L., & Schefuß, E. (2018). Hybrid insolation forcing of Pliocene monsoon dynamics in West Africa. *Climate of the Past*, *14*(1), 73–84. https://doi.org/10.5194/cp-14-73-2018

Larrasoaña, J. C., Roberts, A. P., & Rohling, E. J. (2008). Magnetic susceptibility of eastern Mediterranean marine sediments as a proxy for Saharan dust supply? *Marine Geology*, *254*(3), 224–229. https://doi.org/10.1016/j.margeo.2008.06.003

Larrasoaña, J. C., Roberts, A. P., Rohling, E. J., Winklhofer, M., & Wehausen, R. (2003). Three million years of monsoon variability over the northern Sahara. *Climate Dynamics*, *21*(7–8), 689–698. https://doi.org/10.1007/s00382-003-0355-z

Latif, M., Dommenget, D., Dima, M., & Grötzner, A. (1999). The role of Indian Ocean Sea surface temperature in forcing east african rainfall anomalies during December–January 1997/98. *Journal of Climate*, *12*(12), 3497–3504. https://doi.org/10.1175/1520-0442(1999)012<3497:TROIOS>2.0.CO;2

Lavielle, M. (2005). Using penalized contrasts for the change-point problem. *Signal Processing*, *85*(8), 1501–1510. https://doi.org/10.1016/j.sigpro.2005.01.012

Lawrence, K., Herbert, T., Brown, C., Raymo, M., & Haywood, A. (2009). High-amplitude variations in North Atlantic sea surface temperature during the early Pliocene warm period. *Paleoceanography*, *24*(2), PA2218. https://doi.org/10.1029/2008PA001669

Lechleitner, F. A., Breitenbach, S. F. M., Rehfeld, K., Ridley, H. E., Asmerom, Y., Prufer, K. M., et al. (2017). Tropical rainfall over the last two millennia: Evidence for a low-latitude hydrologic seesaw. *Scientific Reports*, *7*(1), 45809. https://doi.org/10.1038/srep45809

Leif, R. N., & Simoneit, B. R. T. (2000). The role of alkenes produced during hydrous pyrolysis of a shale. *Organic Geochemistry*, *31*(11), 1189–1208. https://doi.org/10.1016/S0146-6380(00)00113-3

Levin, N. E., Zipser, E. J., & Cerling, T. E. (2009). Isotopic composition of waters from Ethiopia and Kenya: Insights into moisture sources for eastern Africa. *Journal of Geophysical Research*, *114*(D23), D23306. https://doi.org/10.1029/2009JD012166

Liddy, H. M., Feakins, S. J., & Tierney, J. E. (2016). Cooling and drying in northeast Africa across the Pliocene. *Earth and Planetary Science Letters*, *449*, 430–438. https://doi.org/10.1016/j.epsl.2016.05.005

Lisiecki, L. E., & Raymo, M. E. (2005). A Pliocene-Pleistocene stack of 57 globally distributed benthic $\delta^{18}O$ records. *Paleoceanography*, *20*(1), n/a. https://doi.org/10.1029/2004PA001071

Lisiecki, L. E., & Raymo, M. E. (2007). Plio–Pleistocene climate evolution: Trends and transitions in glacial cycle dynamics. *Quaternary Science Reviews*, *26*(1–2), 56–69. https://doi.org/10.1016/j.quascirev.2006.09.005

Lourens, L. J., Antonarakou, A., Hilgen, F. J., Hoof, A. A. M. V., Vergnaud-Grazzini, C., & Zachariasse, W. J. (1996). Evaluation of the Plio-Pleistocene astronomical timescale. *Paleoceanography*, *11*(4), 391–413. https://doi.org/10.1029/96PA01125

Lupien, R. L., Russell, J. M., Feibel, C., Beck, C., Castañeda, I., Deino, A., & Cohen, A. S. (2018). A leaf wax biomarker record of early Pleistocene hydroclimate from West Turkana, Kenya. *Quaternary Science Reviews*, *186*, 225–235. https://doi.org/10.1016/j.quascirev.2018.03.012

Lupien, R. L., Russell, J. M., Pearson, E. J., Castañeda, I. S., Asrat, A., Foerster, V., et al. (2022). Orbital controls on eastern African hydroclimate in the Pleistocene. *Scientific Reports*, *12*(1), 3170. https://doi.org/10.1038/s41598-022-06826-z

Lupien, R. L., Russell, J. M., Subramanian, A., Kinyanjui, R., Beverly, E. J., Uno, K. T., et al. (2021). Eastern African environmental variation and its role in the evolution and cultural change of Homo over the last 1 million years. *Journal of Human Evolution*, *157*, 103028. https://doi.org/10.1016/j.jhevol.2021.103028

Lupien, R. L., Russell, J. M., Yost, C. L., Kingston, J. D., Deino, A. L., Logan, J., et al. (2019). Vegetation change in the Baringo Basin, east Africa across the onset of Northern Hemisphere glaciation 3.3–2.6 Ma. *Palaeogeography, Palaeoclimatology, Palaeoecology*, *570*, 109426. https://doi.org/10.1016/j.palaeo.2019.109426

Macgregor, D. (2015). History of the development of the East African Rift System: A series of interpreted maps through time. *Journal of African Earth Sciences*, *101*, 232–252. https://doi.org/10.1016/j.jafrearsci.2014.09.016

Mann, H. B., & Whitney, D. R. (1947). On a test of whether one of two random variables is stochastically larger than the other. *The Annals of Mathematical Statistics*, *18*(1), 50–60. https://doi.org/10.1214/aoms/1177730491

Mantsis, D. F., Lintner, B. R., Broccoli, A. J., Erb, M. P., Clement, A. C., & Park, H.-S. (2014). The response of large-scale circulation to obliquity-induced changes in meridional heating gradients. *Journal of Climate*, *27*(14), 5504–5516. https://doi.org/10.1175/JCLI-D-13-00526.1

Martin, H. A., & McMinn, A. (1994). Late Cainozoic vegetation history of North-Western Australia, from the palynology of a deep sea core (ODP Site 765). *Australian Journal of Botany*, *42*(1), 95–102. https://doi.org/10.1071/bt9940095

Martínez-Garcia, A., Rosell-Melé, A., McClymont, E. L., Gersonde, R., & Haug, G. H. (2010). Subpolar link to the emergence of the modern equatorial Pacific cold tongue. *Science*, *328*(5985), 1550–1553. https://doi.org/10.1126/science.1184480

Marzi, R., Torkelson, B. E., & Olson, R. K. (1993). A revised carbon preference index. *Organic Geochemistry*, *20*(8), 1303–1306. https://doi.org/10.1016/0146-6380(93)90016-5

Maslin, M. A., Brierley, C. M., Milner, A. M., Shultz, S., Trauth, M. H., & Wilson, K. E. (2014). East African climate pulses and early human evolution. *Quaternary Science Reviews*, *101*, 1–17. https://doi.org/10.1016/j.quascirev.2014.06.012

McClymont, E. L., Elmore, A. C., Kender, S., Leng, M. J., Greaves, M., & Elderfield, H. (2016). Pliocene-Pleistocene evolution of sea surface and intermediate water temperatures from the southwest Pacific. *Paleoceanography*, *31*(6), 895–913. https://doi.org/10.1002/2016PA002954

Medina-Elizalde, M., Lea, D. W., & Fantle, M. S. (2008). Implications of seawater Mg/Ca variability for Plio-Pleistocene tropical climate reconstruction. *Earth and Planetary Science Letters*, *269*(3), 585–595. https://doi.org/10.1016/j.epsl.2008.03.014

Minkara, K. (2017). *Zeolite facies and environmental change in the Plio-Pleistocene Baringo Basin, Kenya Rift*. Georgia State University. Retrieved from https://scholarworks.gsu.edu/geosciences_theses/110

Mischell, E., & Lee, J.-E. (2022). Observed zonal variations of the relationship between ITCZ position and meridional temperature contrast. *Climate*, *10*(3), 30. https://doi.org/10.3390/cli10030030

Mitsunaga, B., Lupien, R. L., Ouertani, S., Stubbs, B., Deino, A. L., Kingston, J. D., et al. (2023). NOAA/WDS paleoclimatology—Baringo-Tugen Hills-Barsemoi, Kenya 3.29-2.58 Ma leaf wax biomarker, hydrogen and carbon isotope, magnetic susceptibility, and Si/Ti data [Dataset]. NOAA National Centers for Environmental Information. https://doi.org/10.25921/NM7T-4P42

Naafs, B. D. A., Voelker, A. H. L., Karas, C., Andersen, N., & Sierro, F. J. (2020). Repeated near-collapse of the Pliocene sea surface temperature gradient in the North Atlantic. *Paleoceanography and Paleoclimatology*, *35*(5), e2020PA003905. https://doi.org/10.1029/2020PA003905

Nicholson, S. E. (1997). An analysis of the enso signal in the tropical Atlantic and Western Indian Oceans. *International Journal of Climatology*, *17*(4), 345–375. https://doi.org/10.1002/(SICI)1097-0088(19970330)17:4<345::AID-JOC127>3.0.CO;2-3

Nicholson, S. E., & Kim, J. (1997). The relationship of the El Niño–Southern Oscillation to African rainfall. *International Journal of Climatology*, *17*(2), 117–135. https://doi.org/10.1002/(SICI)1097-0088(199702)17:2<117::AID-JOC84>3.0.CO;2-O

Nutz, A., Schuster, M., Boës, X., & Rubino, J.-L. (2017). Orbitally-driven evolution of Lake Turkana (Turkana Depression, Kenya, EARS) between 1.95 and 1.72 Ma: A sequence stratigraphy perspective. *Journal of African Earth Sciences*, *125*, 230–243. https://doi.org/10.1016/j.jafrearsci.2016.10.016

O'Brien, C. L., Foster, G. L., Martínez-Botí, M. A., Abell, R., Rae, J. W. B., & Pancost, R. D. (2014). High sea surface temperatures in tropical warm pools during the Pliocene. *Nature Geoscience*, *7*(8), 606–611. https://doi.org/10.1038/ngeo2194

Ogega, O. M., Koske, J., Kung'u, J. B., Scoccimarro, E., Endris, H. S., & Mistry, M. N. (2020). Heavy precipitation events over East Africa in a changing climate: Results from CORDEX RCMs. *Climate Dynamics*, *55*(3), 993–1009. https://doi.org/10.1007/s00382-020-05309-z

O'Mara, N. A., Skonieczny, C., McGee, D., Winckler, G., Bory, A. J.-M., Bradtmiller, L. I., et al. (2022). Pleistocene drivers of Northwest African hydroclimate and vegetation. *Nature Communications*, *13*(1), 3552. https://doi.org/10.1038/s41467-022-31120-x

Orsi, A. H., Whitworth, T., & Nowlin, W. D. (1995). On the meridional extent and fronts of the Antarctic Circumpolar Current. *Deep Sea Research Part I: Oceanographic Research Papers*, *42*(5), 641–673. https://doi.org/10.1016/0967-0637(95)00021-W

Otto-Bliesner, B. L., Russell, J. M., Clark, P. U., Liu, Z., Overpeck, J. T., Konecky, B., et al. (2014). Coherent changes of southeastern equatorial and northern African rainfall during the last deglaciation. *Science*, *346*(6214), 1223–1227. https://doi.org/10.1126/science.1259531

Owen, R. B., Muiruri, V. M., Lowenstein, T. K., Renaut, R. W., Rabideaux, N., Luo, S., et al. (2018). Progressive aridification in East Africa over the last half million years and implications for human evolution. *Proceedings of the National Academy of Sciences*, *115*(44), 11174–11179. https://doi.org/10.1073/pnas.1801357115

Partridge, T. C., Demenocal, P. B., Lorentz, S. A., Paiker, M. J., & Vogel, J. C. (1997). Orbital forcing of climate over South Africa: A 200,000-year rainfall record from the Pretoria Saltpan. *Quaternary Science Reviews*, *16*(10), 1125–1133. https://doi.org/10.1016/S0277-3791(97)00005-X

Pausata, F. S. R., Zhang, Q., Muschitiello, F., Lu, Z., Chafik, L., Niedermeyer, E. M., et al. (2017). Greening of the Sahara suppressed ENSO activity during the mid-Holocene. *Nature Communications*, *8*(1), 16020. https://doi.org/10.1038/ncomms16020

Polissar, P. J., Rose, C., Uno, K. T., Phelps, S. R., & deMenocal, P. (2019). Synchronous rise of African C_4 ecosystems 10 million years ago in the absence of aridification. *Nature Geoscience*, *12*(8), 657–660. https://doi.org/10.1038/s41561-019-0399-2

Pond, K. L., Huang, Y., Wang, Y., & Kulpa, C. F. (2002). Hydrogen isotopic composition of individual n-alkanes as an intrinsic tracer for bioremediation and source identification of petroleum contamination. *Environmental Science & Technology*, *36*(4), 724–728. https://doi.org/10.1021/es011140r

Poore, H. R., Samworth, R., White, N. J., Jones, S. M., & McCave, I. N. (2006). Neogene overflow of northern component water at the Greenland-Scotland Ridge. *Geochemistry, Geophysics, Geosystems*, *7*(6), Q06010. https://doi.org/10.1029/2005GC001085

Potts, R., Dommain, R., Moerman, J. W., Behrensmeyer, A. K., Deino, A. L., Riedl, S., et al. (2020). Increased ecological resource variability during a critical transition in hominin evolution. *Science Advances*, *6*(43), eabc8975. https://doi.org/10.1126/sciadv.abc8975

Regenberg, M., Nürnberg, D., Steph, S., Groeneveld, J., Garbe-Schönberg, D., Tiedemann, R., & Dullo, W.-C. (2006). Assessing the effect of dissolution on planktonic foraminiferal Mg/Ca ratios: Evidence from Caribbean core tops. *Geochemistry, Geophysics, Geosystems*, *7*(7), Q07P15. https://doi.org/10.1029/2005GC001019

Reynolds, R. W., Smith, T. M., Liu, C., Chelton, D. B., Casey, K. S., & Schlax, M. G. (2007). Daily high-resolution-blended analyses for sea surface temperature. *Journal of Climate*, *20*(22), 5473–5496. https://doi.org/10.1175/2007JCLI1824.1

Riesselman, C. R., & Dunbar, R. B. (2013). Diatom evidence for the onset of Pliocene cooling from AND-1B, McMurdo Sound, Antarctica. *Palaeogeography, Palaeoclimatology, Palaeoecology*, *369*, 136–153. https://doi.org/10.1016/j.palaeo.2012.10.014

Rodgers, K. B., Latif, M., & Legutke, S. (2000). Sensitivity of equatorial Pacific and Indian Ocean watermasses to the position of the Indonesian Throughflow. *Geophysical Research Letters*, *27*(18), 2941–2944. https://doi.org/10.1029/1999GL002372

Rose, C., Polissar, P. J., Tierney, J. E., Filley, T., & deMenocal, P. B. (2016). Changes in northeast African hydrology and vegetation associated with Pliocene–Pleistocene sapropel cycles. *Philosophical Transactions of the Royal Society B: Biological Sciences*, *371*(1698), 20150243. https://doi.org/10.1098/rstb.2015.0243

Rossignol-Strick, M. (1983). African monsoons, an immediate climate response to orbital insolation. *Nature*, *304*(5921), 46–49. https://doi.org/10.1038/304046a0

Rossignol-Strick, M. (1985). Mediterranean Quaternary sapropels, an immediate response of the African monsoon to variation of insolation. *Palaeogeography, Palaeoclimatology, Palaeoecology*, *49*(3), 237–263. https://doi.org/10.1016/0031-0182(85)90056-2

Rozanski, K., Araguás-Araguás, L., & Gonfiantini, R. (2013). Isotopic patterns in modern global precipitation. In *Climate change in continental isotopic records* (pp. 1–36). American Geophysical Union (AGU). Retrieved from https://agupubs.onlinelibrary.wiley.com/doi/abs/10.1029/GM078p0001

Ruan, Y., Mohtadi, M., van der Kaars, S., Dupont, L. M., Hebbeln, D., & Schefuß, E. (2019). Differential hydro-climatic evolution of East Javanese ecosystems over the past 22,000 years. *Quaternary Science Reviews*, *218*, 49–60. https://doi.org/10.1016/j.quascirev.2019.06.015

Sachse, D., Billault, I., Bowen, G. J., Chikaraishi, Y., Dawson, T. E., Feakins, S. J., et al. (2012). Molecular paleohydrology: Interpreting the hydrogen-isotopic composition of lipid biomarkers from photosynthesizing organisms. *Annual Review of Earth and Planetary Sciences*, *40*(1), 221–249. https://doi.org/10.1146/annurev-earth-042711-105535

Saji, N. H., Goswami, B. N., Vinayachandran, P. N., & Yamagata, T. (1999). A dipole mode in the tropical Indian Ocean. *Nature*, *401*(6751), 360–363. https://doi.org/10.1038/43854

Sarnthein, M., Bartoli, G., Prange, M., Schmittner, A., Schneider, B., Weinelt, M., et al. (2009). Mid-Pliocene shifts in ocean overturning circulation and the onset of Quaternary-style climates. *Climate of the Past*, *5*(2), 269–283. https://doi.org/10.5194/cp-5-269-2009

Sarnthein, M., Grunert, P., Khélifi, N., Frank, M., & Nürnberg, D. (2018). Interhemispheric teleconnections: Late Pliocene change in Mediterranean outflow water linked to changes in Indonesian Through-Flow and Atlantic Meridional Overturning Circulation, a review and update. *International Journal of Earth Sciences*, *107*(2), 505–515. https://doi.org/10.1007/s00531-017-1505-6

Schimmelmann, A., Sessions, A. L., & Mastalerz, M. (2006). Hydrogen Isotopic (D/H) composition of organic matter during diagenesis and thermal maturation. *Annual Review of Earth and Planetary Sciences*, *34*(1), 501–533. https://doi.org/10.1146/annurev.earth.34.031405.125011

Sessions, A. L., Burgoyne, T. W., & Hayes, J. M. (2001). Determination of the H_3 factor in hydrogen isotope ratio monitoring mass spectrometry. *Analytical Chemistry*, *73*(2), 200–207. https://doi.org/10.1021/ac000488m

Sessions, A. L., Sylva, S. P., Summons, R. E., & Hayes, J. M. (2004). Isotopic exchange of carbon-bound hydrogen over geologic timescales. *Geochimica et Cosmochimica Acta*, *68*(7), 1545–1559. https://doi.org/10.1016/j.gca.2003.06.004

Shackleton, N., & Hall, M. A. (1990). Pliocene oxygen isotope stratigraphy of Hole 709C. *Proceedings of the Ocean Drilling Program, Scientific Results*, *115*, 529–538. https://doi.org/10.2973/odp.proc.sr.115.174.1990

Shanahan, T. M., McKay, N. P., Hughen, K. A., Overpeck, J. T., Otto-Bliesner, B., Heil, C. W., et al. (2015). The time-transgressive termination of the African Humid Period. *Nature Geoscience*, *8*(2), 140–144. https://doi.org/10.1038/ngeo2329

Shongwe, M. E., van Oldenborgh, G. J., van den Hurk, B., & van Aalst, M. (2011). Projected changes in mean and extreme precipitation in Africa under global warming. Part II: East Africa. *Journal of Climate*, *24*(14), 3718–3733. https://doi.org/10.1175/2010JCLI2883.1

Shultz, S., Nelson, E., & Dunbar, R. I. M. (2012). Hominin cognitive evolution: Identifying patterns and processes in the fossil and archaeological record. *Philosophical Transactions of the Royal Society B: Biological Sciences*, *367*(1599), 2130–2140. https://doi.org/10.1098/rstb.2012.0115

Sier, M. J., Dupont-Nivet, G., Langereis, C., Deino, A. L., Kingston, J. D., & Cohen, A. S. (2021). Magnetostratigraphy of the Hominin Sites and Paleolakes Drilling Project (HSPDP) Baringo-Tugen Hills-Barsemoi core (Kenya). *Palaeogeography, Palaeoclimatology, Palaeoecology*, *570*, 110190. https://doi.org/10.1016/j.palaeo.2020.110190

Simon, M. H., Ziegler, M., Bosmans, J., Barker, S., Reason, C. J. C., & Hall, I. R. (2015). Eastern South African hydroclimate over the past 270,000 years. *Scientific Reports*, *5*(1), 18153. https://doi.org/10.1038/srep18153

Skonieczny, C., McGee, D., Winckler, G., Bory, A., Bradtmiller, L. I., Kinsley, C. W., et al. (2019). Monsoon-driven Saharan dust variability over the past 240,000 years. *Science Advances*, *5*(1), eaav1887. https://doi.org/10.1126/sciadv.aav1887

Smith, R. A., & Castañeda, I. S. (2020). NOAA/WDS paleoclimatology—Eastern Indian Ocean biomarker data and sea surface temperature reconstructions from 3.5—1.5 Ma [Dataset]. NOAA National Centers for Environmental Information. https://doi.org/10.25921/E1P0-9T22

Taylor, A. K., Berke, M. A., Castañeda, I. S., Koutsodendris, A., Campos, H., Hall, I. R., et al. (2021). Plio-Pleistocene continental hydroclimate and Indian Ocean sea surface temperatures at the Southeast African Margin. *Paleoceanography and Paleoclimatology*, *36*(3), e2020PA004186. https://doi.org/10.1029/2020PA004186

Tiedemann, R., Sarnthein, M., & Shackleton, N. (1994). Astronomic timescale for the Pliocene Atlantic $\delta^{18}O$ and dust flux records of Ocean Drilling Program Site 659. *Paleoceanography*, *9*(4), 619–638. https://doi.org/10.1029/94PA00208

Tierney, J. E., deMenocal, P. B., & Zander, P. D. (2017). A climatic context for the out-of-Africa migration. *Geology*, *45*(11), 1023–1026. https://doi.org/10.1130/G39457.1

Tierney, J. E., Lewis, S. C., Cook, B. I., LeGrande, A. N., & Schmidt, G. A. (2011). Model, proxy and isotopic perspectives on the East African Humid Period. *Earth and Planetary Science Letters*, *307*(1), 103–112. https://doi.org/10.1016/j.epsl.2011.04.038

Tierney, J. E., Smerdon, J. E., Anchukaitis, K. J., & Seager, R. (2013). Multidecadal variability in East African hydroclimate controlled by the Indian Ocean. *Nature*, *493*(7432), 389–392. https://doi.org/10.1038/nature11785

Tierney, J. E., & Tingley, M. P. (2015). A TEX_{86} surface sediment database and extended Bayesian calibration. *Scientific Data*, *2*(1), 1–10. https://doi.org/10.1038/sdata.2015.29

Trauth, M. H. (2021). Spectral analysis in Quaternary sciences. *Quaternary Science Reviews*, *270*, 107157. https://doi.org/10.1016/j.quascirev.2021.107157

Trauth, M. H., Larrasoaña, J. C., & Mudelsee, M. (2009). Trends, rhythms and events in Plio-Pleistocene African climate. *Quaternary Science Reviews*, *28*(5), 399–411. https://doi.org/10.1016/j.quascirev.2008.11.003

Trauth, M. H., Maslin, M. A., Deino, A., & Strecker, M. R. (2005). Late Cenozoic moisture history of east Africa. *Science*, *309*(5743), 2051–2053. https://doi.org/10.1126/science.1112964

Trauth, M. H., Maslin, M. A., Deino, A. L., Strecker, M. R., Bergner, A. G. N., & Dühnforth, M. (2007). High- and low-latitude forcing of Plio-Pleistocene East African climate and human evolution. *Journal of Human Evolution*, *53*(5), 475–486. https://doi.org/10.1016/j.jhevol.2006.12.009

Ummenhofer, C. C., Gupta, A. S., England, M. H., & Reason, C. J. C. (2009). Contributions of Indian Ocean sea surface temperatures to enhanced East African rainfall. *Journal of Climate*, *22*(4), 993–1013. https://doi.org/10.1175/2008JCLI2493.1

van der Lubbe, H. J. L., Hall, I. R., Barker, S., Hemming, S. R., Baars, T. F., Starr, A., et al. (2021). Indo-Pacific Walker circulation drove Pleistocene African aridification. *Nature*, *598*(7882), 618–623. https://doi.org/10.1038/s41586-021-03896-3

Verosub, K. L., & Roberts, A. P. (1995). Environmental magnetism: Past, present, and future. *Journal of Geophysical Research*, *100*(B2), 2175–2192. https://doi.org/10.1029/94JB02713

Vuille, M., Werner, M., Bradley, R. S., Chan, R. Y., & Keimig, F. (2005). Stable isotopes in East African precipitation record Indian Ocean zonal mode. *Geophysical Research Letters*, *32*(21), L21705. https://doi.org/10.1029/2005GL023876

Wara, M. W., Ravelo, A. C., & Delaney, M. L. (2005). Permanent El Niño-like conditions during the Pliocene warm period. *Science*, *309*(5735), 758–761. https://doi.org/10.1126/science.1112596

Webster, P. J., Moore, A. M., Loschnigg, J. P., & Leben, R. R. (1999). Coupled ocean–atmosphere dynamics in the Indian Ocean during 1997–98. *Nature*, *401*(6751), 356–360. https://doi.org/10.1038/43848

Westover, K. S., Stone, J. R., Yost, C. L., Scott, J. J., Cohen, A. S., Rabideaux, N. M., et al. (2021). Diatom paleolimnology of late Pliocene Baringo Basin (Kenya) paleolakes. *Palaeogeography, Palaeoclimatology, Palaeoecology*, *570*, 109382. https://doi.org/10.1016/j.palaeo.2019.109382

Wichura, H., Bousquet, R., Oberhänsli, R., Strecker, M. R., & Trauth, M. H. (2010). Evidence for middle Miocene uplift of the East African Plateau. *Geology*, *38*(6), 543–546. https://doi.org/10.1130/G31022.1

Windler, G., Tierney, J. E., & deMenocal, P. B. (2023). Hydroclimate variability in the equatorial western Indian Ocean for the last 250,000 years. *Paleoceanography and Paleoclimatology*, *38*(2), e2022PA004530. https://doi.org/10.1029/2022PA004530

WoldeGabriel, G., Haile-Selassie, Y., Renne, P. R., Hart, W. K., Ambrose, S. H., Asfaw, B., et al. (2001). Geology and palaeontology of the Late Miocene Middle Awash valley, Afar rift, Ethiopia. *Nature*, *412*(6843), 175–178. https://doi.org/10.1038/35084058

Yemane, K., Bonnefille, R., & Faure, H. (1985). Palaeoclimatic and tectonic implications of Neogene microflora from the Northwestern Ethiopian highlands. *Nature*, *318*(6047), 653–656. https://doi.org/10.1038/318653a0

Yost, C. L., Ivory, S. J., Deino, A. L., Rabideaux, N. M., Kingston, J. D., & Cohen, A. S. (2021). Phytoliths, pollen, and microcharcoal from the Baringo Basin, Kenya reveal savanna dynamics during the Plio-Pleistocene transition. *Palaeogeography, Palaeoclimatology, Palaeoecology*, *570*, 109779. https://doi.org/10.1016/j.palaeo.2020.109779

Ziegler, M., Simon, M. H., Hall, I. R., Barker, S., Stringer, C., & Zahn, R. (2013). Development of Middle Stone Age innovation linked to rapid climate change. *Nature Communications*, *4*(1), 1905. https://doi.org/10.1038/ncomms2897